On the growth of microtubule asters spanning millimeter-sized cells

Citation

Permanent link

Terms of Use

Share Your Story

On the growth of microtubule asters spanning millimeter-sized cells

Dissertation advisor: Professor Timothy J. Mitchison   Keisuke Ishihara

On the growth of microtubule asters spanning millimeter-sized cells

Abstract

The large cells in early vertebrate embryos are organized by radial arrays of microtubules called asters. Asters grow, interact, and move to precisely position the cleavage planes of for each cell division. Cell-spanning dimensions are presumably required for interphase asters to explore the size and shape of the large cytoplasm. It has been unclear whether asters grow to fill the enormous egg according to the standard model of aster growth proposed in smaller somatic cells, or whether special mechanisms are required. In this dissertation, I combine biochemical reconstitution and biophysical modeling to propose a new model of aster growth that involves autocatalytic microtubule nucleation. By imaging asters in a cell-free system derived from frog eggs, I measure the number and positions of microtubules over time and find that most microtubules were nucleated away from the centrosome. I also find the interphase egg cytoplasm supports spontaneous nucleation after a time lag. Given these observations, I construct a biophysical model that describes aster growth from the interplay of microtubule polymerization dynamics and autocatalytic nucleation. This leads to the concept of a critical nucleation rate, which defines the quantitative conditions that predicts either (i) a growing aster characterized by a linear increase radius without dilution of microtubule density at the periphery, or (ii) a steady-state aster with small, constant radius. By combining theory and experiments, I propose a scenario where unbounded aster growth consists of individual microtubules that are themselves bounded in length. This offers a mechanistic explanation to how cells might differentially regulate aster size during the cell cycle. In summary, aster growth is a collective phenomenon of microtubules providing us with insight to how cells self-organize.

Contents

Listing of figures

Citations to Current or Previously Published Works

With minor alterations to standardize their format, chapters of this dissertation were taken in its entirety from the following papers or manuscripts:

CHAPTER 1

"Organization of early frog embryos by chemical waves emanating from centrosomes"
Keisuke Ishihara, Phuong A. Nguyen, Martin Wühr, Aaron C. Groen, Christine M. Field and Timothy J. Mitchison
published in Phil. Trans. R. Soc. B. 369:2013.0454 (2014)

CHAPTER 2

"Microtubule nucleation remote from centrosomes may explain how asters span large cells"
Keisuke Ishihara, Phuong A. Nguyen, Aaron C. Groen, Christine M. Field, and Timothy J. Mitchison
published in Proc. Natl. Acad. Sci. U.S.A. 111:17715-17722 (2014)

CHAPTER 3

"Physical basis of microtubule aster growth"
Keisuke Ishihara, Kirill S. Korolev, and Timothy J. Mitchison
manuscript in preparation

I dedicate this dissertation to my parents.

Acknowledgments

THIS DISSERTATION, would not have been possible without the support of many people.

I spent my formative period as a scientist at Musashi Junior and Senior High School. Our Chemistry Club coach, Akira Takaesu, was a true scientist-educator. He would lead the club to his home field, the Manza hot springs, and we analyzed the water and volcanic gases. For my independent project concerning the reaction of concentrated sulfuric acid and sucrose, he would always encourage me to try things and see things for myself, while he carried out his own experiments in the room next door.

As a chemical engineering student at Princeton, I was introduced to modern biology with a strong quantitative emphasis through the Integrated Science curriculum taught by David Botstein, Eric Wieschaus, Josh Rabinowitz and Leonid Kruglyak. I thank Coleen Murphy and Amy Caudy for their research guidance for our junior year Project Lab. I thank Yoosik Kim and Stas Shvartsman for their mentorship during my thesis research. It was also in Stas' seminar class that I encountered a biophysical model describing microtubule dynamic instability as a biased random walk.

From the first days in the Mitchison lab, Tim treated me as an independent colleague than a student. His love for experiments was truly contagious. I thank him for being the most encouraging

For every type of animal there is a most convenient size,
and a large change in size inevitably carries with it a
change of form.

J.B.S. Haldane, *On Being the Right Size*

0

Introduction - Microtubule asters were discovered in large embryonic cells

ASTERS AND CENTROSOMES were discovered by the early cytologists of the late 19th century. While Edouard van Beneden was the first to report the radial mitotic structures inside fertilized eggs of the roundworm parasite *Ascaris megalocephala* (Van Beneden, 1887), Theodor Boveri observed the same cells and coined the term "centrosomes" to describe the cellular body at the center of astral rays. Recognizing the importance of this organelle, Boveri wrote in 1887 that "the centrosome represents the dynamic centre of the cell; its division creates the centres of the forming daughter
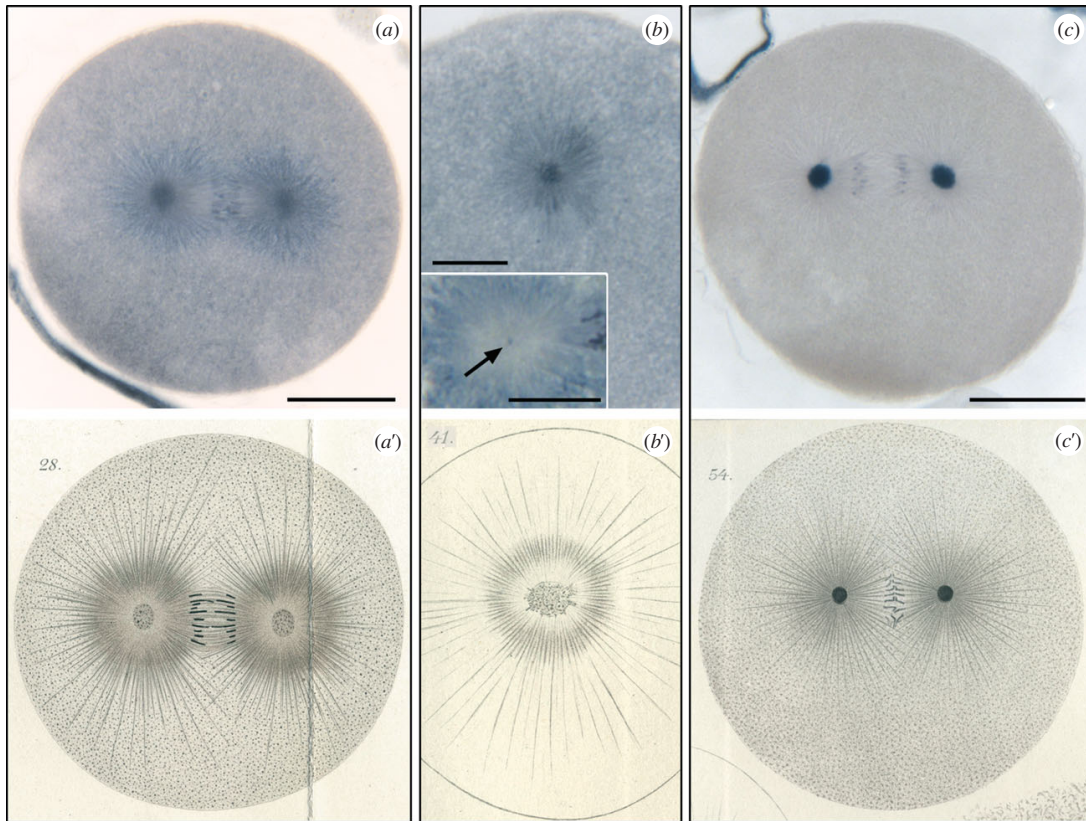
Figure 0.1: **Asters and centrosomes during the first division of the sea urchin *Echinus microtuberculatus* eggs.** One of the earliest observations of asters and centrosomes by Theodor Boveri in 1887. Comparison between Boveri's drawings (a'-c') and photographs taken from Boveri's original slides (a-d). Scale bars, (a-c) 20 mm and (inset in b) 10 mm. Reprinted with permission from (Scheer, 2014).

cells, around which all other cellular components arrange themselves symmetrically[...] The centrosome is the true division organ of the cell, it mediates the nuclear and cellular division" (Boveri, 1887; 1888; Scheer, 2014). During his visit to the Zoological Station in Naples the following year, Boveri observed live sea urchin eggs (Figure 0.1) where the incorporated sperm forms an aster ('Strahlensonne', or radiating sun), strengthening his convictions. Boveri directly influenced the American cell biologist E.B. Wilson, who described the basic functions and morphologies of asters in his seminal book (Wilson, 1896).

Today, we know that microtubule asters are essential for the spatial organization of animal cells. During cell division, the mitotic spindle is positioned parallel to the long axis of the cell (Hertwig, 1893) with the aid of astral microtubules. When two asters interact, they direct the position of furrow (Rappaport, 1961). Cells can differentiate through asymmetric division, which requires the spindle to be off-centered by astral microtubules pulling on the cortex (reviewed in Neumüller and Knoblich, 2009). During fertilization, asters facilitate pronuclear fusion, where the male and female pronuclei find each other by follow the aster's rays (Chambers, 1939). In interphase cells, asters position the nucleus and centrosome at the cell center. The efficient formation of endoplasmic reticulum membrane networks relies on interphase microtubules (Waterman-Storer and Salmon, 1998). Finally, astral microtubules support cell motility through vesicle trafficking, signaling, mechanical support (Etienne-Manneville, 2013). These diverse functions are enabled by microtubule aster's key property: how it spans the length of the cell.

This dissertation concerns the mechanism of how microtubule asters grow. In particular, I focus on the growth of microtubule asters that spatially organize large embryonic cells. While this is the classic context in which asters were discovered over a century ago, the extreme physical challenges faced by these cells have been overlooked. I argue that the widely accepted model of aster growth fails to explain how asters rapidly span millimeter-sized cytoplasms during the short cleavage cycles. By combining biochemical reconstitution, quantitative imaging and theory, I propose a new model in which large aster growth is explained by autocatalytic nucleation of short, dynamic microtubules. Thus, aster growth is a collective phenomenon of microtubules, providing a stellar example for us to understand how cells self-organize.

0.1 Asters are composed of microtubules that undergo polymerization dynamics

Cytoskeletal dynamics is at the heart of how we understand cells today. However, it was not until the mid 20th century that biologists began to appreciate cell physiology as the consequence of the dynamics properties inherent to the fibers that compose cellular structures. At the time, the main structures that could be observed in living cells via phase contrast microscopy were chromosomes and nucleoli. This led to a heated debate among researchers, some of which questioned the importance and existence of the mitotic spindle by rejecting them as mere fixation artifacts. This controversy was resolved by Shinya Inoue's efforts in applying a drastically improved form of polarized light microscopy, which allowed him to definitely show that the spindle was composed of aligned protein fibers in living cells (Inoué and Dan, 1951; Inoué, 1953 and Figure 0.2). By studying the dynamic response of mitotic structures under normal and physicochemically perturbed conditions, Inoue proposed the "dynamic equilibrium model" for spindle and astral fibers (Inoué and Sato, 1967), explaining their dynamic rearrangements through reversible polymerization and depolymerization.

The pioneering biophysical concepts put forth by Inoue and colleagues were soon supported by other major findings in cell biology. First, aided by improved fixation methods, pioneers of electron microscopy reported the common presence of hollow cellular structures not limited to mitosis, giving rise to the unified nomenclature of "microtubules" (Ledbetter and Porter, 1963; Slautterback, 1963). Second, Gary Borisy and Ed Taylor identified the direct binding target of colchicine (later named "tubulin") and proposed it as the subunit of microtubules (Borisy and Taylor, 1967a; b). Microtubules were soon assembled from purified tubulin (Weisenberg, 1972). Thus, the structural and biochemical basis of microtubules as dynamic polymers were established. This series of events culminated in the discovery of dynamic instability of microtubule growth (Mitchison and Kirschner, 1984), and forms one of the most important foundations of modern cell physiology.
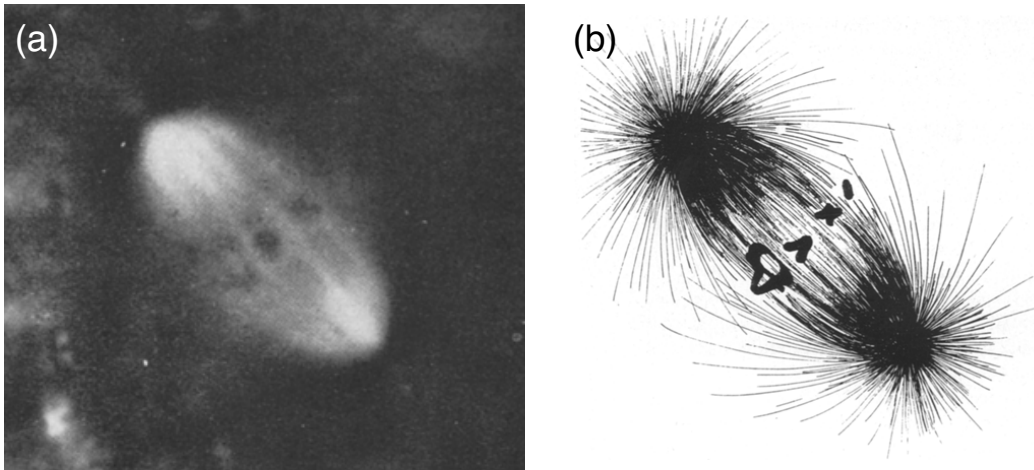
Figure 0.2: **Mitotic spindle and astral rays observed in a living oocyte of parchment worm** *Chaetopterus perga-mentaee.* Shinya Inoue pioneered live imaging in cell biology with polarized light microscopy, which allowed him to study the dynamic nature of spindle fibers and astral rays. Polscope image (a) and its trace in negative projection (b). Reprinted with permission from (Inoué, 1953).

0.2 MODELS FOR ASTER GROWTH - THE RADIAL ELONGATION MODEL AND BEYOND

How microtubule asters grow is a fundamental problem in cell organization. The standard model, which I refer to as the radial elongation model, posits that centrosomes nucleate and anchor microtubules at their minus ends while plus ends extend into the cytoplasm by dynamic instability. This model was strongly supported by studies in cultured mammalian cells that used electron microscopy to examine microtubules emerging from pericentrosomal material (reviewed in Brinkley, 1985). Microtubule regrowth assays indicated centrosomes were the preferred nucleation sites in cells (Brinkley et al., 1967). Pure tubulin and isolated centrosomes were demonstrated to be sufficient for assembling the stereotypical radial morphology (Weisenberg and Rosenfeld, 1975), further supporting the radial elongation model.

While radial elongation represents the textbook model for aster growth, reports of non-centrosomal microtubules challenge the dominant role of centrosomes for microtubule assembly and organization. Several mechanisms have been documented to generate microtubules whose minus ends are

not directly anchored to the centrosome (Keating and Borisy, 1999). Microtubules may be released from the centrosome and transported outward by motor proteins (Keating et al., 1997; Waterman-Storer et al., 2000). Microtubules may be broken into multiple shorter pieces either by mechanical force or severing enzymes (reviewed in Roll-Mecak and McNally, 2010). Microtubules also nucleate spontaneously in the cytoplasm (Vorobjev et al., 1997), from the Golgi apparatus (reviewed in Zhu and Kaverina, 2013), or from pre-existing microtubules (Clausen and Ribbeck, 2007; Petry et al., 2013). These observations come from a variety of cell types including epithelial cells, neurons, and muscle cells, which have specialized microtubule organizations that support their unique cellular functions. The relative importance of centrosomes in organizing microtubules varies with cell type, suggesting alternative modes of aster growth.

One of the greatest remaining mysteries of microtubule biology is arguably the process of nucleation. In contrast to microtubule plus end dynamics and motor-mediated transport that have been extensively studied at the molecular and biophysical levels, microtubule nucleation is still poorly understood. First of all, the birth of a microtubule from tubulin subunits, which possibly exist as diffusible oligomers, is not well defined. Even when markers that specifically bind to growing plus ends are imaged, tracking and scoring whether the plus end originated from a centrosome or elsewhere is a non-trivial problem in image analysis. While the gamma-tubulin ring complex has been proposed as the physiological template for nucleation (reviewed in Kollman et al., 2011), how it is activated and whether the complex is an absolute requirement for nucleation are still open questions. Finally, perturbations that affect microtubule plus end dynamics often influence nucleation (Groen et al., 2009) and confound experimental interpretation. For these reasons, we currently lack a mechanistic understanding of how microtubule nucleation, especially at sites distal from centrosomes, contributes to the microtubule organization inside living cells.

0.3 Growth of large interphase asters in fish and frog embryos

Some of the largest microtubule asters are observed in the rapidly dividing cells of early fish and amphibian embryos. During interphase, asters grow rapidly until they reache the cortex (Wühr et al., 2008; 2009). Cytoplasmically anchored dynein pulls on the astral microtubules and move the aster, positioning the site of spindle assembly at the center of the cell (Wühr et al., 2010). When two asters interact, they form a specialized zone of antiparallel microtubule overlaps (Wühr et al., 2010; Nguyen et al., 2014), which recruits molecular factors that instructs when and where the actin contractile ring should assemble. Thus, the microtubule asters play a central role in the spatial organization of large dividing cells.

How such large microtubule asters grow is unknown. The radial elongation model predicts the microtubule density to drop at the aster periphery, but the density appears to be constant or even increasing with radial distance in fixed images (Wühr et al., 2008; 2010). It is difficult to explain this pattern of microtubules without assuming the existence of microtubules whose minus ends are not anchored to the centrosome. How are non-centrosomal microtubules generated and how do they contribute to aster growth? How do we explain the rapid, linear rate at which the aster radius increases, when individual microtubules are undergoing dynamic instability?

In this dissertation, I employ two synergistic approaches to explain large aster growth. The first approach is biochemical reconstitution. Rather than studying intact cells, I prepare undiluted cytoplasm and use centrosome mimics to assemble asters under a cover slip. This demonstrates that aster growth does not require the cell cortex, chromatin or even centrosomes, but is a consequence of the self-organizing nature of the cytoplasm. The *in vitro* reaction makes the problem of aster growth accessible to a variety of sophisticated imaging techniques and precise biochemical perturbations. The second approach is biophysical modeling. I construct and analyze an idealized model of aster growth, capturing the essence of aster growth. Even in the absence of known molecular factors, the

biophysical model offers a mechanistic understanding of aster growth as an emergent property of the underlying microscopic processes.

The scope of dissertation is as follows. In Chapter 1, I introduce the concept of chemical waves as a physical principle that enables the rapid spatiotemporal organization of large cytoplasms observed in early embryos. Drawing on the literature suggesting the centrosome as an initiator for cell cycle waves, I present the hypothesis of microtubule aster growth as a propagating wave of autocatalytic microtubule nucleation. Chapter 2 reports our study of aster growth by cell-free reconstitution using the *Xenopus* egg extract system. The reconstitution approach identifies non-centrosomal microtubule nucleation as a key process underlying large aster growth. In Chapter 3, I present a biophysical model of aster growth that couples microtubule dynamic instability and autocatalytic nucleation. The model qualitatively recapitulates large aster growth and offers a mechanistic explanation to how cells might differentially regulate aster size according to the cell cycle.

References

Borisy, G.G., and E.W. Taylor. 1967a. The mechanism of action of colchicine. Binding of colchincine-3H to cellular protein. The Journal of cell biology. 34:525-533.

Borisy, G.G., and E.W. Taylor. 1967b. The mechanism of action of colchicine. Colchicine binding to sea urchin eggs and the mitotic apparatus. The Journal of cell biology. 34:535-548.

Boveri, T. 1887. Ueber den Antheil des Spermatozoon an der Theilung des Eies.

Boveri, T. 1888. Zellenstudien II. Die Befruchtung und Teilung des Eies von Ascaris megalocephala. Jena. Zeitschr. Naturwiss.

Brinkley, B.R. 1985. Microtubule organizing centers. Annu. Rev. Cell Biol. 1:145-172.

Brinkley, B.R., E. Stubblefield, and T.C. Hsu. 1967. The effects of colcemid inhibition and reversal on the fine structure of the mitotic apparatus of Chinese hamster cells *in vitro*. J. Ultrastruct. Res. 19:1-18.

Chambers, E.L. 1939. The movement of the egg nucleus in relation to the sperm aster in the echinoderm egg. Journal of Experimental Biology.

Clausen, T., and K. Ribbeck. 2007. Self-organization of anastral spindles by synergy of dynamic instability, autocatalytic microtubule production, and a spatial signaling gradient. PLoS ONE. 2:e244.

Etienne-Manneville, S. 2013. Microtubules in Cell Migration. Annu. Rev. Cell Dev. Biol. 29:471-499.

Groen, A.C., T.J. Maresca, J.C. Gatlin, E.D. Salmon, and T.J. Mitchison. 2009. Functional overlap of microtubule assembly factors in chromatin-promoted spindle assembly. Mol Biol Cell. 20:2766-2773.

Hertwig, O. 1893. Ueber den Wert der ersten Furchungszellen für die Organbildung des Embryos. Arch. f. mikr. Anat.

Inoué, S. 1953. Polarization optical studies of the mitotic spindle. I. The demonstration of spindle fibers in living cells. Chromosoma. 5:487-500.

Inoué, S., and H. Sato. 1967. Cell motility by labile association of molecules. The nature of mitotic

spindle fibers and their role in chromosome movement. J. Gen. Physiol. 50:Suppl:259-92.

Inoué, S., and K. Dan. 1951. Birefringence of the dividing cell. Journal of Morphology.

Keating, T.J., and G.G. Borisy. 1999. Centrosomal and non-centrosomal microtubules. Biol. Cell. 91:321-329.

Keating, T.J., J.G. Peloquin, V.I. Rodionov, D. Momcilovic, and G.G. Borisy. 1997. Microtubule release from the centrosome. Proceedings of the National Academy of Sciences of the United States of America. 94:5078-5083.

Kollman, J.M., A. Merdes, L. Mourey, and D.A. Agard. 2011. Microtubule nucleation by gamma-tubulin complexes. Nat Rev Mol Cell Biol. 12:709-721.

Ledbetter, M.C., and K.R. Porter. 1963. A "Microtubule" In Plant Cell Fine Structure. The Journal of cell biology. 19:239-250.

Mitchison, T., and M. Kirschner. 1984. Dynamic instability of microtubule growth. Nature.

Neumüller, R.A., and J.A. Knoblich. 2009. Dividing cellular asymmetry: asymmetric cell division and its implications for stem cells and cancer. Genes Dev. 23:2675-2699.

Nguyen, P.A., A.C. Groen, M. Loose, K. Ishihara, M. Wühr, C.M. Field, and T.J. Mitchison. 2014. Spatial organization of cytokinesis signaling reconstituted in a cell-free system. Science. 346:244-247.

Petry, S., A.C. Groen, K. Ishihara, T.J. Mitchison, and R.D. Vale. 2013. Branching microtubule nucleation in *Xenopus* egg extracts mediated by augmin and TPX2. Cell. 152:768-777.

Rappaport, R. 1961. Experiments concerning the cleavage stimulus in sand dollar eggs. J. Exp. Zool. 148:81-89.

Roll-Mecak, A., and F.J. McNally. 2010. Microtubule-severing enzymes. Curr Opin Cell Biol. 22:96-103.

Scheer, U. 2014. Historical roots of centrosome research: discovery of Boveri's microscope slides in Wurzburg. Philosophical Transactions of the Royal Society B: Biological Sciences. 369:20130469-20130469.

Slautterback, D.B. 1963. Cytoplasmic Microtubules. I. Hydra. The Journal of cell biology. 18:367-388.

Van Beneden, E. 1887. Nouvelles recherches sur la fécondation et la division mitosique chez l'Ascaride mégalocéphale.

Vorobjev, I.A., T.M. Svitkina, and G.G. Borisy. 1997. Cytoplasmic assembly of microtubules in cultured cells. J Cell Sci. 110 (Pt21):2635-2645.

Waterman-Storer, C., D.Y. Duey, K.L. Weber, J. Keech, R.E. Cheney, E.D. Salmon, and W.M. Bement. 2000. Microtubules remodel actomyosin networks in *Xenopus* egg extracts via two mechanisms of F-actin transport. The Journal of cell biology. 150:361-376.

Waterman-Storer, C.M., and E.D. Salmon. 1998. Endoplasmic reticulum membrane tubules are distributed by microtubules in living cells using three distinct mechanisms. Curr Biol. 8:798-806.

Weisenberg, R.C. 1972. Microtubule formation *in vitro* in solutions containing low calcium concentrations. Science. 177:1104-1105.

Weisenberg, R.C., and A.C. Rosenfeld. 1975. *In vitro* polymerization of microtubules into asters and spindles in homogenates of surf clam eggs. The Journal of cell biology. 64:146-158.

Wilson, E.B. 1896. The Cell in development and inheritance. Macmillan, New York. 1 pp.

Wühr, M., E.S. Tan, S.K. Parker, H.W. Detrich, and T.J. Mitchison. 2010. A model for cleavage plane determination in early amphibian and fish embryos. Curr Biol. 20:2040-2045.

Wühr, M., S. Dumont, A.C. Groen, D.J. Needleman, and T.J. Mitchison. 2009. How does a millimeter-sized cell find its center? Cell Cycle. 8:1115-1121.

Wühr, M., Y. Chen, S. Dumont, A.C. Groen, D.J. Needleman, A. Salic, and T.J. Mitchison. 2008. Evidence for an upper limit to mitotic spindle length. Curr Biol. 18:1256-1261.

Zhu, X., and I. Kaverina. 2013. Golgi as an MTOC: making microtubules for its own good. Histochem. Cell Biol. 140:361-367.

Every discourse, even a poetic or oracular sentence,
carries with it a system of rules for producing analogous
things and thus an outline of methodology.

Jacques Derrida

1

How do frog eggs self-organize?

CITATION

"Organization of early frog embryos by chemical waves emanating from centrosomes"

Keisuke Ishihara, Phuong A. Nguyen, Martin Wühr, Aaron C. Groen, Christine M. Field and Timothy J. Mitchison

published in Phil. Trans. R. Soc. B. 369:2013.0454 (2014)

ABSTRACT

The large cells in early vertebrate development face an extreme physical challenge in organizing their cytoplasm. For example, amphibian embryos have to divide cytoplasm that spans hundreds of microns every 30 minutes according to a precise geometry, a remarkable accomplishment given the extreme difference between molecular and cellular scales in this system. How do the biochemical reactions occurring at the molecular scale lead to this emergent behavior of the cell as a whole? Based on recent findings, we propose that the centrosome plays a crucial role by initiating two autocatalytic reactions that travel across the large cytoplasm as chemical waves. Waves of mitotic entry and exit propagate out from centrosomes using the Cdk1 oscillator to coordinate the timing of cell division. Waves of microtubule-stimulated microtubule nucleation propagate out to assemble large asters that position spindles for the following mitosis and establish cleavage plane geometry. By initiating these chemical waves, the centrosome rapidly organizes the large cytoplasm during the short embryonic cell cycle, which would be impossible using more conventional mechanisms such as diffusion or nucleation by structural templating. Large embryo cells provide valuable insights to how cells control chemical waves, which may be a general principle for cytoplasmic organization.

Physical extremes in biology are interesting. They may reveal special mechanisms, or under-appreciated aspects of widespread mechanisms. Here, we address the challenges faced by cells -frog zygotes and early blastomeres- that are extremely large, but need to divide rapidly. *Xenopus laevis* eggs are 1.2 mm in diameter, and they divide every 30 min. These numbers represent extraordinary challenges in terms of spatial and temporal organization: How can a millimeter-scale cell be spatially patterned by nanometer-scale molecules? How can a cell that would take a protein hours to cross by diffusion alone generate the precisely controlled timing required for cell cycle progression on a scale of minutes? We argue, based on observations by others (Chang and Ferrell, 2013) and our group (Wühr et al., 2008; 2010; Mitchison et al., 2012), that these spatial and temporal organizational challenges may be solved by a common class of biophysical mechanism: chemical reaction waves, also called "trigger waves" (Chang and Ferrell, 2013). Furthermore, the centrosome plays a key role in organizing these waves, and can be re-imagined as a wave-initiating site.

A chemical reaction wave is a special case in kinetic organization of dissipative dynamical systems. It requires an excitable medium that locally amplifies a chemical state so the state can propagate through the medium faster than diffusion. Familiar examples include the Belousov-Zhabotinsky reaction (Zhabotinsky, 1991), action potential in neurons (Bullock et al., 1977), calcium waves during fertilization (Whitaker, 2006) and cAMP waves in a population of Dictyostelium cells (Tomchik and Devreotes, 1981; Gregor et al., 2010). Microtubule organization and cell cycle progression are not normally considered as chemical waves, apart from few notable exceptions (Masui, 1972; Pérez-Mongiovi et al., 1998; Tabony and Job, 1990; Mandelkow and Mandelkow, 1992). We will argue this is an interesting way to think about their spatiotemporal organization in frog zygotes, and that chemical waves are perhaps the only way the huge zygote cell can self-organize in space and time. By extension, we believe chemical waves may be much more prevalent inside cells than has been

thought, and may play important roles in organizing small (Loose et al., 2008; Weiner et al., 2006; Goehring et al., 2011) as well as large cells.

The centrosome plays a special role in our hypothesis as an initiator. Chemical waves can occur spontaneously in excitable media, but in many cases a defined initiation site provides a trigger or catalyst to initiate waves. As the wave propagates outwards, it carries spatial information on the location of the initiator to distant sites. In this way, we believe, the centrosome informs the mm-sized frog egg of the location of its center. Chemical waves allow this spatial information transfer to occur in minutes, even in the millimeter-scale cytoplasm. It would take many hours by diffusion alone, and might be impractical by microtubule polymerization alone. The centrosome was defined in the 19th century as the center of the cell largely based on observation of large embryo cells (Boveri, 1888; Wilson, 1925). In the 1980s its role as a microtubule nucleation template was established (Brinkley, 1985). Since then it has been viewed as organizing cells primarily by templating minus ends using γ-tubulin complexes. The centrosome has also been implicated in cell cycle control. We propose that the centrosome coordinates space and time in extremely large cells by initiating chemical waves of cell cycle progression (Chang and Ferrell, 2013) and microtubule organization [this review]. We write to provoke discussion, with the warning that some of our ideas are quite speculative. In the spirit of this volume we hope to generate feedback and new experiments. Even if only partially correct, the idea that the centrosome functions as a chemical wave initiator is an interesting new way to think about spatiotemporal organization of cells.

1.2   Chemical waves - the basics

Pattern formation by reaction-diffusion systems has foundations in physics and chemical engineering, but has broad implications to epidemiology, ecology and cell biology (reviewed in Murray, 2002). It represents a general class of mathematical models that explains how patterns arise from collective interactions occurring at much smaller scales. Turing famously analyzed a pair of interacting,

diffusible chemical species and derived the conditions that give rise to spontaneous emergence of apparently stable, periodic patterns, providing a hypothetical conceptual basis for morphogenesis long before any morphogens had been identified (Turing, 1952). Here, following the early works of Luther (Luther, 1987), Fisher (Fisher, 1937) and Kolmogorov (Kolmogorov and Petrovskii, 1937), we use the example of a simple one component system that conveys the essence of how reaction-diffusion systems generate transient waves inside cells. Imagine that the cytoplasm exists anywhere between the "On" and "Off" state of some biochemical activity, in our case, mitotic Cdk1 kinase activity and microtubule assembly (Figure 1.1a), and that this activity can vary over time and space. The medium may support transient waves if the following two requirements are met: (i) an autocatalytic reaction exists which promotes the "On" state and (ii) reactant transport occurs, for example by molecular diffusion, but other transport processes could substitute. A prototypical example of an autocatalytic reaction is the logistic growth model, in which a chemical species increases exponentially and saturates. Starting with an initial concentration restricted in space, growth (rate α [min^{-1}]) in the absence of any transport will predict this local region to increase ("On") while the rest of the system remains "Off" (Figure 1.1b). With a similar initial condition, diffusion (D [μm^2 min^{-1}] alone will predict the gradual homogenization of reactants (Figure 1.1c). However, when growth and diffusion occur simultaneously and satisfy quantitative conditions, the system gives rise to a moving front that travels at a linear speed of order $\sqrt{4D\alpha}$ [$\mu\text{m min}^{-1}$] (Luther, 1987; Fisher, 1937; Kolmogorov and Petrovskii, 1937) (Figure 1.1d). As the front passes through a given location, the state of the cytoplasm is converted from the "Off" to the "On" state. At the microscopic level, this could be understood as a cascade of active molecules diffusing into adjacent space to induce more activity. With more complex oscillatory reactions, this mechanism may result in pulsing or spiral patterns. Importantly, this phenomenon is observed in a continuous medium of arbitrary size and shape. To describe the dynamic patterns that emerge in reaction-diffusion systems in cells, we will use the term "chemical waves" to emphasize the biochemical nature of the cytoplasm.
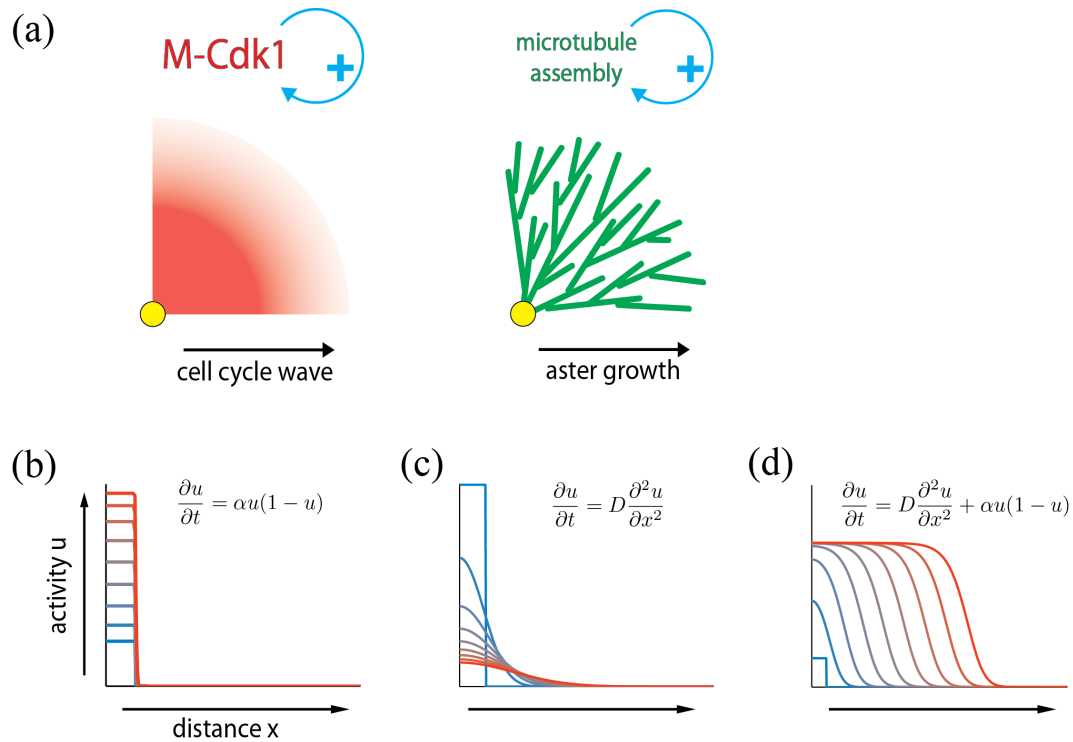
Figure 1.1: **Chemical waves initiated by the centrosome.** (a) In our hypothesis, the centrosome (yellow circle) triggers two types of autocatalytic reactions that spread radially outward through the cytoplasm. Cell cycle waves are mediated by mitotic Cdk1 feedback regulation, while aster growth is mediated by microtubule-stimulated microtubule assembly. (b-d) Requirements of the cytoplasm to support chemical waves. Curves show spatiotemporal dynamics of biochemical activity according to the equations shown, which are non-unique examples of each situation. (b) Growth, or an autocatalytic reaction, with saturation results in local amplification of activity. (c) Diffusion results in the homogenization of activity. (d) When growth and diffusion are coupled, a propagating front, or a chemical wave, may be observed. Equations are shown for the one-dimensional case, but the long time scale prediction of a propagating wave front is remarkably robust for higher dimensions, radial geometry and a range of initial conditions. Note that the logistic growth term in (d) represents a broad class of reactions with positive feedback, including the growth phase of excitable/bistable kinetics.

Due to their ability to rapidly communicate information across space without a predefined blueprint, chemical waves have great potential as the physical basis supporting cellular physiology. This may be particularly useful for large cells, where simple diffusion of signaling molecules would be too slow. For example, a typical protein with a cytoplasmic diffusion coefficient of $D = 500$ [$\mu\text{m}^2 \text{ min}^{-1}$] (Salmon et al., 1984; Elowitz et al., 1999) would take hours to travel from the center to the periphery of a frog egg with radius 600 μm (time $t = L^2/6D = 120$ min). In contrast, cell cycle waves traverse similar distances in minutes (Chang and Ferrell, 2013; Hara et al., 1980) and calcium waves in tens of seconds (Whitaker, 2006). This can be understood by assuming an autocatalytic reaction of rate 1 [min^{-1}], resulting in a chemical wave of speed $\sqrt{4D\alpha} = \sqrt{4 \cdot 500 \cdot 1} = 45$ [$\mu\text{m min}^{-1}$], which will travel the same distance in 13 min. Despite its rapid, adaptable properties, chemical waves possess potential drawbacks. In addition to requiring particular biochemistry and energy dissipation, excitable systems are prone to spontaneous waves triggered by fluctuations in local concentrations. This presents a challenge in adopting chemical waves for highly coordinated physiological processes such as cell division, since spontaneous initiation would defeat the purpose of a spatial organizing system. One strategy to mitigate this issue is to implement a strong, nonlinear negative feedback into the system, which increases the threshold for activation. Another non-exclusive strategy is to robustly and quickly initiate the reaction at a controlled location and allow the chemical wave to sweep through large space before any spontaneous waves occur. In this scenario, the initiator's role is analogous to that of the conductor in an orchestra who instructs the correct timing of biochemical reactions with a common signal that spreads across the cell. For both cell cycle progression and microtubule organization, we argue that the centrosome acts as the initiator for these chemical waves, albeit by poorly understood mechanisms. In the following sections, we discuss how cell cycle progression and microtubule aster organization are coordinated in the early frog embryo. To critically evaluate the hypothesis that chemical waves emanating from centrosomes form the physical basis of these phenomena, we ask if the systems exhibit two key characteristics of

chemical waves: (1) the cytoplasm supports autocatalytic reactions (2) these reactions rapidly propagate activity through space without dilution. We also ask if, and how, the centrosome functions as an initiator.

1.3   CELL CYCLE PROGRESSION AS A CHEMICAL WAVE

The discovery of surface contraction waves (SCWs) in large amphibian zygotes is perhaps the earliest observation of cell cycle states propagating through the cytoplasm. In time-lapse images of fertilized eggs made in the 1970s, Hara observed a traveling wave of cortical contraction, visualized by movement of pigment granules. These SCWs occurred just before the first cleavage and proceeded as circular waves from the animal to the vegetal pole (Hara, 1970; Hara et al., 1980) (Figure 1.2a). SCWs consists of two distinct waves: SCWa was the result of the relaxation of the cortical tension, while the succeeding SCWb was a stiffening of the cortex (Yoneda et al., 1982). The two sets of waves occurred periodically corresponding to the period of normal cleavage cycle in developing embryos (Hara et al., 1980), suggesting they were a manifestation of cell cycle control of cytoskeletal behavior (Hara et al., 1980; Christensen and Merriam, 1982; Field et al., 2011). Subsequent research demonstrated that increase and decrease in mitotic Cdk1 activity was responsible for the onset of SCWa and SCWb (Rankin and Kirschner, 1997; Pérez-Mongiovi et al., 1998), suggesting that SCWs are mitotic entry and exit waves, respectively. SCWs that travel across the millimeter cytoplasm in early amphibian embryos are a dramatic example of cell cycle regulation in space. Cell cycle waves have also been reported in other large cells (Hara, 1971; Houliston et al., 1993). They fulfill one important criterion for chemical waves in that they travel at near constant velocity without dilution of activity, but these data alone do not establish that the egg is an excitable medium for cell cycle progression.

What is the molecular basis of the cell cycle waves traveling across large amphibian eggs? The biochemical clock that generates sustained cycles of division is centered on Cyclin B-Cdk1 kinase activity (reviewed in Morgan, 2007; Ferrell, 2013). This system oscillates due to continuous synthesis and
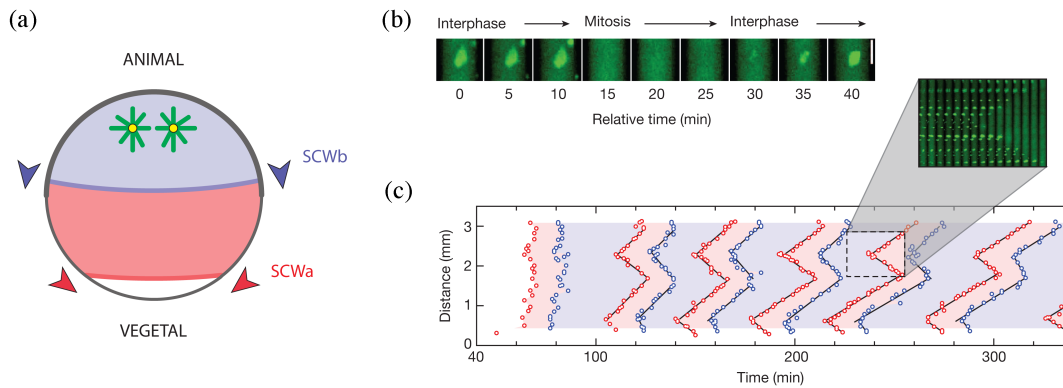
Figure 1.2: **Cell cycle waves in large cytoplasm.** (a) In fertilized frog embryos, surface contraction waves (SCWs) travel from the animal to the vegetal pole. Regions of high (pink) and low (purple) mitotic Cdk1 activity co-exist in the common cytoplasm. Centrosomes (yellow) reside in the animal half of the embryo until the eight-cell stage. Illustration adapted from (Beckhelling et al., 2000). (b-c) Reconstitution of cell cycle waves in cycling *Xenopus* egg extract filled in a Teflon tube. Reprinted by permission from Macmillan Publishers Ltd: Nature (Chang and Ferrell, 2013), copyright 2013. (b) Cell cycle state is monitored by nuclear envelope dynamics with GFP fused to nuclear localization sequence. (c) Spatial dynamics of cell cycle inside tube of length 3 mm. Nuclear envelope breakdown (red points) and reformation (blue points) indicates whether the cytoplasm is in mitosis (pink) or interphase (purple). The sloped lines indicate cell cycle waves and their velocities.

periodic destruction of Cyclin B, and harbors positive feedback of kinase activation by the Cdc25C phosphatase and Wee1A/Myt1 kinase. The potential for chemical waves of mitotic activation in this system had been noted (Pérez-Mongiovi et al., 1998; Novak and Tyson, 1993). In a recent report, Chang and Ferrell proved that waves can indeed occur by combining in silico and in vitro experiments (Chang and Ferrell, 2013). Using computer simulations to model the spatial changes in cell cycle state, they showed that a locally elevated activity of Cdk1 should propagate through a large cytoplasm as a chemical wave. The propagation speed of such waves is predicted by the kinetics of the cell cycle oscillator and diffusion of proteins, and was estimated to be 40-120 μm min^{-1}, which is in similar order with the speed of SCWs at 60 μm min^{-1} observed in vivo. Next, the propagation of cell cycle waves was reconstituted in a cell-free system by filling Teflon tubes with cycling egg extract supplemented with sperm nuclei. To monitor cell cycle progression, times of nuclear envelope assembly and breakdown were recorded (Figure 1.2b). After the first synchronous cycle, the center of

the tube first started to enter mitosis and this spread laterally across the entire tube at 60 μm min^{-1} (Figure 1.2c). Multiple pairs of mitotic entry and exit waves were observed in the same reaction over time. Inhibition of Wee1A/Myt1 accelerated the wave speeds in a dose dependent manner underscoring the fact that the strength of autocatalysis imposed on Cdk1 activity is an important parameter for the speed of these waves. As the extract contained multiple nuclei and centrosomes in these experiments, it is difficult to draw conclusions on how their presence affected the kinetics of cell cycle progression. However, the striking finding from Chang and Ferrell's work was that the cytoplasmic oscillator responsible for cell cycle progression is sufficient to generate chemical waves that temporally organize a large cytoplasm.

SCWs are initiated in the animal half of the zygote, suggesting the presence of an initiation site. Accumulating evidence suggests that the centrosome initiates the mitotic entry wave. Injection of purified centrosomes accelerates mitotic entry in frog and starfish oocytes (Pérez-Mongiovi et al., 2000; Picard et al., 1987) consistent with an initiator role. Spindle pole bodies, the centrosome equivalent in fission yeast, are known to promote entry into mitosis (Bridge et al., 1998; Petersen and Hagan, 2005; Fong et al., 2010). In somatic cells, active Cyclin B-Cdk1 concentrates on the centrosome in early prophase (Jackman et al., 2003), and centrosomal recruitment of the Cdc25C phosphatase may be responsible for this initial activation (Bonnet et al., 2008). The centrosome could also act indirectly, by positioning the nucleus, which then acts as the proximal trigger of mitotic entry waves. The nucleus is thought to amplify mitotic Cdk1 activity through compartmentalization (Pines and Hunter, 1991; Gallant and Nigg, 1992). In this view, the centrosome and nucleus may together establish the perinuclear region as a robust initiation site for the mitotic entry wave (Chang and Ferrell, 2013). Finally, we note that the nucleus and the animal half cytoplasm initiate SCW in the absence of centrosomes (Hara et al., 1980; Pérez-Mongiovi et al., 2000). Therefore, it is likely that the additive effects of the centrosome, nucleus and the animal half cytoplasm ensure the robust initiation of the cell cycle in the animal half of the zygote.

In embryos (Yoneda et al., 1982) and egg extract (Chang and Ferrell, 2013), a mitotic exit wave follows the mitotic entry wave, and has a similar velocity (Figure 1.2c). Whether mitotic exit is a self-sustaining autocatalytic reaction that can generate waves, and if so what determines their velocity, remain to be determined. Feedback between Cdk1 and the anaphase-promoting complex/cyclosome (APC/C) through XErp1 (Tischer et al., 2012; Vinod et al., 2013; Ferrell, 2013) presents a potential autocatalytic mechanism for a mitotic exit, but it is not clear why this different reaction would propagate with the same velocity as the entry wave. An alternative is that the exit wave is a consequence of local changes in the cytoplasm that follows the mitotic entry wave with a fixed time delay (Rankin and Kirschner, 1997), and therefore does not need to be autocatalytic or capable of wave propagation in its own. In either model the centrosome may influence the kinetics. In human cells and early fly embryos, Cyclin B-GFP localizes on spindles and starts to disappear first near the spindle poles in anaphase (Huang and Raff, 1999; Wakefield et al., 2000; Clute and Pines, 1999). Thus, during mitotic exit, APC/C activity may be initiated at centrosomes and then propagate outwards.

1.4 Radial organization of microtubules as a chemical wave

The cell cycle wave discussed above presumably exists to synchronize the cell cycle across a large cell, rather than transmit positional information. We propose that microtubule asters also grow by a chemical wave mechanism in large embryo cells and, in this case, the goal is spatial organization, and correct positioning of cleavage planes. In frog eggs, microtubule asters are small in mitosis due to high Cdk1 activity which limits microtubule growth (Belmont et al., 1990; Verde et al., 1992) (Figure 1.3b). When Cdk1 activity decreases following fertilization, or anaphase onset, asters grow out rapidly from centrosomes. The sperm aster grows to fill the whole cell (Figure 1.3a), while anaphase asters fill half the cell, since they do not interpenetrate across the mid-plane (Figure 1.3cd) (Wühr et al., 2009; 2010; Mitchison et al., 2012). The outer edge of the aster expands at approximately 30 μm min^{-1} in *Xenopus* zygotes, and approximately 15 μm min^{-1} in zebrafish 1st mitosis (Wühr et

al., 2008; 2010). This rapid growth is essential for the aster to fill the whole cell in time to position the centrosomes for the following mitosis, and also to trigger cleavage furrow ingression following anaphase. Ingression initiates when, and where, the overlap zone between the two asters expands to touch the cortex. Presumably, the aster-aster interaction results from the collective action of microtubule-associated proteins that specifically modulate the dynamics of antiparallel bundles (Mitchison et al., 2012), and is beyond the scope of the chemical wave model presented in this article. In addition to growing rapidly, we believe it is important that microtubules in the aster are not spatially diluted as the asters grow. Initiating a furrow presumably requires signaling from some sufficient density of microtubules, and images in frog and fish embryos suggest that the aster retains an approximately constant microtubule density at its periphery as it expands (Figure 1.3d). Propagation at a constant, rapid rate and lack of dilution during propagation are two of the hallmarks of chemical waves.

The standard model for aster growth, which we call the radial elongation model, is illustrated in Figure 1.3e. Microtubules are nucleated with their minus ends anchored at the centrosome, and addition of GTP tubulin at plus ends promotes aster growth. In this geometry, the density of microtubules must decrease with radial distance r (density scales as $1/r$ in 2-D or $1/r^2$ in 3-D). However, immunofluorescence images from frog embryos show that the microtubule network at the aster periphery has a bushy appearance, and its density appears to be constant, or even increase, with aster radius (Figure 1.3d). Movies from zebrafish provided a similar appearance (Wühr et al., 2010). Given this microtubule distribution, it seems highly unlikely that all microtubule minus ends are anchored at the centrosome. We propose instead that microtubule nucleation occurs within the growing aster away from the centrosome (Wühr et al., 2009), and that nucleation is stimulated by pre-existing microtubules (Figure 1.3f). In support of this hypothesis, there is accumulating evidence for microtubule nucleation at non-centrosomal sites associated with pre-existing microtubules. In the cortex of higher plant cells, microtubules nucleate from γ-tubulin ring complexes attached to the side of
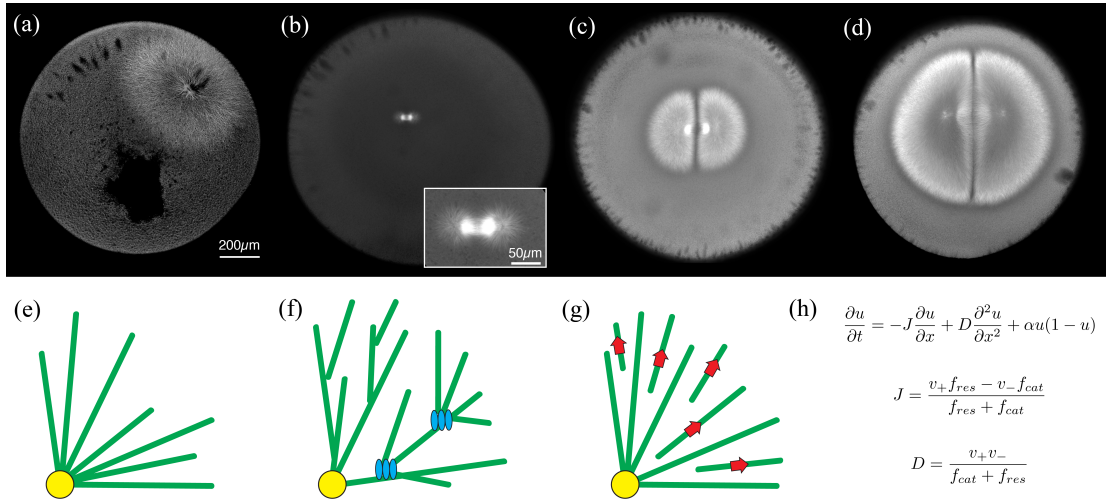
Figure 1.3: Growth of microtubule asters in the large interphase cytoplasm of frog zygotes. (a-d) Growth and interaction of asters in the first division in *Xenopus laevis*. Fertilized eggs were fixed, stained for tubulin and imaged from the animal pole by a confocal microscope as described (Wühr et al., 2008; 2010). (a) Sperm aster during the interphase following fertilization. The sperm aster eventually covers the entire cytoplasm. (b) Metaphase of first mitosis (spindle magnified in inset). Aster size is limited at spindle poles. (c) anaphase-telophase of first mitosis. Aster growth and interaction between asters originating from the same spindle. (d) Later telophase. Note the dense, bushy appearance of microtubules at the aster periphery, low microtubule density in the interaction zone. (e-g) Models for aster growth in large cells. (e) Conventional radial elongation model. Microtubules polymerize outward from centrosomes (yellow). Microtubule density at the aster periphery decreases. (f) Nucleation away from the centrosome may occur on pre-existing microtubules or Golgi membranes (blue stacks). (g) Release and outward transport. Minus ends are released from the centrosomal nucleation site and microtubules slide outward (red arrows). (h) Reaction-diffusion model of microtubule aster expansion. v_+, v_- are rates of polymerization and depolymerization. f_{cat} and f_{res} are catastrophe and rescue frequencies of the microtubule plus end.

other microtubules (Murata et al., 2005; Nakamura et al., 2010). A similar self-amplifying micro-tubule nucleation process was demonstrated in *Xenopus* egg extracts arrested in meiotic metaphase, by a poorly understood process requiring Augmin/HAUS complex (Petry et al., 2013). The mor-phology of interphase aster growth is consistent with parallel nucleation templated from the walls of existing microtubules, but other hypotheses cannot be excluded at present. For example, micro-tubules might activate a kinase that locally promotes nucleation, as is seen for Aurora B kinase ac-tivity in meiotic metaphase (Sampath et al., 2004; Kelly et al., 2007). The Golgi apparatus nucleates microtubules in interphase somatic cells (Chabin-Brion et al., 2001; Efimov et al., 2007; Rivero et al., 2009), including neurons (Ori-McKenney et al., 2012) and muscle cells (Oddoux et al., 2013). Pre-existing microtubule could accumulate Golgi membranes and thus enhance nucleation. Whatever the molecular mechanism, several observations suggest the interphase cytoplasm maybe an excitable medium for microtubule assembly. Electrically activated eggs, where no centrosome is introduced, form asters (Elinson and Rowning, 1988; Houliston and Elinson, 1991) and furrow (Briggs and King, 1953). Enucleated, activated eggs also form microtubule asters spontaneously (Houliston and Elin-son, 1991). Thus microtubules eventually form, and perhaps expand as asters, in the absence of cen-trosomes or nuclei. Even following normal fertilization, microtubules assemble at the vegetal cortex to promote rotation of the cytoplasm relative to the cortex, and this population can form sponta-neously (Elinson and Paleček, 1993). Thus, the interphase cytoplasm does fulfill one property for an excitable medium: spontaneous formation of microtubules when the initiation site is not present.

Self-amplification of microtubules should prevent dilution of microtubule density in radial ge-ometries. An interesting question is whether this has a kinetic contribution; in other words, does this accelerate aster expansion? Though we notice that the rates of microtubule polymerization and that of aster expansion are of comparable magnitude, microtubules in interphase asters evidently depolymerize (Wühr et al., 2010 and our unpublished results). In one model of dynamic instability (Mitchison and Kirschner, 1984), the transitions of microtubule plus ends between the growing and

shrinking states have been modeled as a biased random walk at long time scales (Verde et al., 1992; Bicout, 1997). The net polymerization rate J is simply the weighted average of the polymerization and depolymerization, where the weighting depends on catastrophe and rescue rates (Figure 1.3h). Though the time-averaged net polymerization rate J is thought to take a positive value in interphase (Verde et al., 1992), it is considerably smaller than the instantaneous polymerization rate of growing plus ends v_+ . This raises the question of how the aster expands at a rate much faster than the net polymerization rate J. The chemical wave hypothesis offers a potential explanation to this apparent discrepancy. In the biased random walk model, the net polymerization rate J contributes through an advective term (aka. bias in direction), while the random walk behavior, characterized by the coefficient D, is present in the diffusive term (Figure 1.3h). It is important to note that the diffusive term does not represent a molecule diffusing through the cytoplasm, but rather the stochastic nature of microtubule plus end positions. When a reaction term corresponding to microtubule nucleation is introduced, the coupling of diffusive process with growth (nucleation rate α) predicts the overall aster expansion velocity V as $V = J + \sqrt{4D\alpha}$. Therefore, the chemical wave model offers a quantitative explanation to how microtubule-stimulated microtubule nucleation and dynamic instability may synergistically contribute to the aster expansion rate. An aster could expand to cell-spanning dimension in this model even if J was negative, as it is in mitosis. J and/or α would have to be correspondingly larger, so the net velocity of aster expansion V was positive.

Applying the prototypical reaction-diffusion equation above was more a conceptual starting point than a truly accurate description of aster growth. Many questions remain regarding the apparently simple process of how a large embryo aster grows. Though centrosomes are obvious candidates as initiators for microtubule waves, it is unknown whether its capability for microtubule nucleation is locally restricted or reach longer distances (Dassow et al., 2009; Cowan and Hyman, 2004). Cytoplasmic dynein is thought to exert outward force on astral microtubules (Wühr et al., 2010), so it is possible that minus ends are released and glide outwards (Figure 1.3g). We have so

far assumed the minus ends formed away from centrosomes are stable, presumably capped by γ-tubulin ring complex (Kollman et al., 2011; Wiese and Zheng, 2006) or the CAMSAP/Patronin family of proteins (Meng et al., 2008; Goodwin and Vale, 2010; Jiang et al., 2014), but they may well be free to depolymerize. The reaction-diffusion model presented above predicts that the aster expansion rate increases indefinitely with nucleation rate, but this seems physically implausible given that microtubules polymerize at finite speed. Reaction-telegraph equations that combine the process of growth and persistent random walk (Méndez et al., 2010; Holmes, 1993) may be better suited for predicting such physical bounds. In any case, we believe that the key to understanding aster growth lies in both the identification the key molecular factors and rigorous evaluation of quantitative models under the framework of chemical waves.

Finally, are the cell cycle and microtubule assembly waves that propagate from centrosomes independent, or are they coordinated in some way? During mitosis, high Cdk1 activity regulates a complex network of microtubule associated proteins, promoting catastrophes and bounding microtubule length (Belmont et al., 1990; Verde et al., 1992). Passage of the mitotic exit wave removes this constraint, and may be sufficient to convert the cytoplasm from non-excitable to excitable for microtubule assembly. Alternatively, aster growth may require time-dependent activation of molecular factors during interphase. In either case, the microtubule polymerization wave depends on prior passage of the mitotic exit wave. It might be possible to co-image the two waves to gain insight into their coordination. In the early zebrafish embryo, actin-associated vesicles change motility behavior as the zygote proceeds from mitosis to interphase, and particles closer to the centrosome are affected earlier than more distal ones (Wühr et al., 2010; Field et al., 2011), suggesting that they are responding to a mitotic exit wave emanating from centrosomes. Importantly, this motility change wave precedes the aster growth wave. In frog eggs, cell cycle waves travel at $60\ \mu\mathrm{m}\ \mathrm{min}^{-1}$, which is faster than the estimated aster growth rate of $30\ \mu\mathrm{m}\ \mathrm{min}^{-1}$. Therefore, a plausible scenario is one in which a preceding mitotic exit wave primes the cytoplasm to support aster growth. We know much

less about interphase aster disassembly at the onset of mitosis. This also needs to occur rapidly, and must relate in time to the mitotic entry wave. In some movies, aster disassembly appears to propagate outwards from the centrosome, suggesting disassembly might also occur as a chemical wave initiated at centrosomes. Whether this wave is the mitotic entry wave, or some downstream biochemistry that depends on mitotic entry, is an interesting question for future study.

1.5 Perspective and Future Directions

Over the past few decades, the centrosome's role in cell cycle control and microtubule organization has been well established. Our proposal is to expand this view and reimagine the centrosome as a chemical wave initiator in the context of large dividing cells. Further investigation of cell cycle waves calls for imaging the cell cycle in space and time at the molecular level. The behaviors of fluorescent probes such as Cyclin B-GFP (Clute and Pines, 1999; Wakefield et al., 2000; Huang and Raff, 1999), Cdk1 activity FRET probes (Gavet and Pines, 2010), cell cycle dependent protein-protein interactions (Niethammer et al., 2007) should be studied in relation to centrosome position and microtubules. Using *Xenopus* egg extract, we have recently developed a system that reconstitutes the growth and interaction of large microtubule asters (Mitchison et al., 2012) and permits high spatiotemporal imaging of microtubule dynamics during aster growth. Candidate factors for microtubule nucleation away from the centrosome can be perturbed by immunodepletion. Another interesting direction of research concerns the cross talk between the chemical waves of cell cycle and microtubule. Observations made in cell-free systems should ultimately be tested in vivo. Microinjection and live imaging performed on the large transparent zebrafish embryos have already advanced our understanding of large asters (Wühr et al., 2010; 2011). The complementary advantages offered by *Xenopus* extracts and zebrafish zygotes will advance our understanding on cell cycle waves and aster growth. Further, it is tempting to speculate if centrosomes initiate other kinds of chemical waves (Cowan and Hyman, 2004; Dassow et al., 2009).

Chemical waves might be the only physically plausible way for large cells to rapidly organize their cytoplasm. Are chemical waves a special property of large cells, or is it an intrinsic capability of the cellular cytoplasm that is underappreciated in smaller cells? Increasing evidence suggests that cytoplasmic patterning by reaction-diffusion mechanisms is widespread in a variety of cells (Bement and Dassow, 2014). In the medium sized C. *C. elegans* embryo, cell polarity is thought arise from an diffusion-advection-reaction mechanism (Goehring et al., 2011). Actin polymerization waves are initiated at the cell periphery and underlie neutrophil chemotaxis (Weiner et al., 2006; 2007). The membrane-bound MinCD proteins oscillate between the poles in tiny bacterial cells (Raskin and de Boer, 1999; Hu and Lutkenhaus, 1999), and their spontaneous surface waves have recently been reconstituted in bulk solution (Loose et al., 2008; 2011). The early Drosophila embryo has been suggested to produce metachronous mitotic waves by coupling biochemical and mechanical excitability (Idema et al., 2013). In all cases, localized initiation is a key design element that allows spatial propagation of information by chemical waves. Studying how large embryos divide with this renewed interest on the centrosome as the initiator will help us understand how chemical wave mechanisms are implemented and conserved to support basic physiological functions across different cell types and organisms.

Acknowledgements

References

Beckhelling, C., D. Pérez-Mongiovi, and E. Houliston. 2000. Localised MPF regulation in eggs. Biol. Cell. 92:245-253.

Belmont, L.D., A.A. Hyman, K.E. Sawin, and T.J. Mitchison. 1990. Real-time visualization of cell cycle-dependent changes in microtubule dynamics in cytoplasmic extracts. Cell. 62:579-589.

Bement, W.M., and G. von Dassow. 2014. ScienceDirectSingle cell pattern formation and transient cytoskeletal arrays. Curr Opin Cell Biol. 26:51-59.

Bicout, D. 1997. Green's functions and first passage time distributions for dynamic instability of microtubules. Physical Review E.

Bonnet, J., P. Coopman, and M.C. Morris. 2008. Characterization of centrosomal localization and dynamics of Cdc25C phosphatase in mitosis. Cell Cycle. 7:1991-1998.

Boveri, T. 1888. Zellenstudien II. Die Befruchtung und Teilung des Eies von Ascaris megalocephala. Jena. Zeitschr. Naturwiss.

Bridge, A.J., M. Morphew, R. Bartlett, and I.M. Hagan. 1998. The fission yeast SPB component Cut12 links bipolar spindle formation to mitotic control. Genes Dev. 12:927-942.

Briggs, R., and T.J. King. 1953. Factors affecting the transplantability of nuclei of frog embryonic cells. J. Exp. Zool. 122:485-505.

Brinkley, B.R. 1985. Microtubule organizing centers. Annu. Rev. Cell Biol. 1:145-172.

Bullock, T.H., R. Orkand, and A.D. Grinnell. 1977. Introduction to Nervous Systems. W.H. Freeman. 1 pp.

Chabin-Brion, K., J. Marceiller, F. Perez, C. Settegrana, A. Drechou, G. Durand, and C. Poüs. 2001. The Golgi complex is a microtubule-organizing organelle. Mol Biol Cell. 12:2047-2060.

Chang, J.B., and J.E. Ferrell. 2013. Mitotic trigger waves and the spatial coordination of the *Xenopus* cell cycle. Nature. 500:603-607.

Christensen, K., and R.W. Merriam. 1982. Insensitivity to cytochalasin B of surface contractions keyed to cleavage in the *Xenopus* egg. J Embryol Exp Morphol. 72:143-151.

Clute, P., and J. Pines. 1999. Temporal and spatial control of cyclin B1 destruction in metaphase. Nature Cell Biology. 1:82-87.

Cowan, C.R., and A.A. Hyman. 2004. Centrosomes direct cell polarity independently of micro-tubule assembly in *C. elegans* embryos. Nature. 431:92-96.

Dassow, von, G., K.J.C. Verbrugghe, A.L. Miller, J.R. Sider, and W.M. Bement. 2009. Action at a distance during cytokinesis. The Journal of cell biology. 187:831-845.

Efimov, A., A. Kharitonov, N. Efimova, J. Loncarek, P.M. Miller, N. Andreyeva, P. Gleeson, N. Galjart, A.R.R. Maia, I.X. McLeod, J.R. Yates, H. Maiato, A. Khodjakov, A. Akhmanova, and I. Kaverina. 2007. Asymmetric CLASP-dependent nucleation of noncentrosomal microtubules at the trans-Golgi network. Dev Cell. 12:917-930.

Elinson, R.P., and B. Rowning. 1988. A transient array of parallel microtubules in frog eggs: potential tracks for a cytoplasmic rotation that specifies the dorso-ventral axis. Dev Biol. 128:185-197.

Elinson, R.P., and J. Paleček. 1993. Independence of two microtubule systems in fertilized frog eggs: the sperm aster and the vegetal parallel array. Roux's archives of developmental biology.

Elowitz, M.B., M.G. Surette, P.E. Wolf, J.B. Stock, and S. Leibler. 1999. Protein mobility in the cytoplasm of Escherichia coli. J. Bacteriol. 181:197-203.

Ferrell, J.E. 2013. Feedback loops and reciprocal regulation: recurring motifs in the systems biology of the cell cycle. Curr Opin Cell Biol.

Field, C.M., M. Wühr, G.A. Anderson, H.Y. Kueh, D. Strickland, and T.J. Mitchison. 2011. Actin behavior in bulk cytoplasm is cell cycle regulated in early vertebrate embryos. J Cell Sci. 124:2086-2095.

Fisher, R. 1937. The Wave of Advance of Advantageous Genes. Annals of Human Genetics. 7:355-369.

Fong, C.S., M. Sato, and T. Toda. 2010. Fission yeast Pcp1 links polo kinase-mediated mitotic entry to gamma-tubulin-dependent spindle formation. EMBO J. 29:120-130.

Gallant, P., and E.A. Nigg. 1992. Cyclin B2 undergoes cell cycle-dependent nuclear translocation and, when expressed as a non-destructible mutant, causes mitotic arrest in HeLa cells. The Journal of cell biology. 117:213-224.

Gavet, O., and J. Pines. 2010. Progressive activation of CyclinB1-Cdk1 coordinates entry to mitosis.

Dev Cell. 18:533-543.

Goehring, N.W., P.K. Trong, J.S. Bois, D. Chowdhury, E.M. Nicola, A.A. Hyman, and S.W. Grill. 2011. Polarization of PAR proteins by advective triggering of a pattern-forming system. Science. 334:1137-1141.

Goodwin, S.S., and R.D. Vale. 2010. Patronin regulates the microtubule network by protecting microtubule minus ends. Cell. 143:263-274.

Gregor, T., K. Fujimoto, N. Masaki, and S. Sawai. 2010. The onset of collective behavior in social amoebae. Science. 328:1021-1025.

Hara, K. 1970. "Double camera" time-lapse micro-cinematography. Simultaneous filming of both poles of the amphibian egg. Mikroskopie. 26:181-184.

Hara, K. 1971. Cinematographic observation of "surface contraction waves" (SCW) during the early cleavage of axolotl eggs. Wilhelm Roux' Archiv. 167:183–186.

Hara, K., P. Tydeman, and M. Kirschner. 1980. A cytoplasmic clock with the same period as the division cycle in *Xenopus* eggs. Proceedings of the National Academy of Sciences of the United States of America. 77:462-466.

Holmes, E.E. 1993. Are diffusion models too simple? A comparison with telegraph models of invasion. American Naturalist. 779-795.

Houliston, E., and R.P. Elinson. 1991. Patterns of microtubule polymerization relating to cortical rotation in *Xenopus laevis* eggs. Development. 112:107-117.

Houliston, E., D. Carré, J.A. Johnston, and C. Sardet. 1993. Axis establishment and microtubule-mediated waves prior to first cleavage in Beroe ovata. Development. 117:75-87.

Hu, Z., and J. Lutkenhaus. 1999. Topological regulation of cell division in Escherichia coli involves rapid pole to pole oscillation of the division inhibitor MinC under the control of MinD and MinE. Mol Microbiol. 34:82-90.

Huang, J., and J.W. Raff. 1999. The disappearance of cyclin B at the end of mitosis is regulated spatially in Drosophila cells. EMBO J. 18:2184-2195.

Idema, T., J.O. Dubuis, L. Kang, M.L. Manning, P.C. Nelson, T.C. Lubensky, and A.J. Liu. 2013. The syncytial Drosophila embryo as a mechanically excitable medium. PLoS ONE. 8:e77216.

Jackman, M., C. Lindon, E.A. Nigg, and J. Pines. 2003. Active cyclin B1-Cdk1 first appears on centrosomes in prophase. Nature Cell Biology. 5:143-148.

Jiang, K., S. Hua, R. Mohan, I. Grigoriev, K.W. Yau, Q. Liu, E.A. Katrukha, A.F.M. Altelaar, A.J.R. Heck, C.C. Hoogenraad, and A. Akhmanova. 2014. Microtubule Minus-End Stabilization by Polymerization-Driven CAMSAP Deposition. Dev Cell. 1-15.

Kelly, A.E., S.C. Sampath, T.A. Maniar, E.M. Woo, B.T. Chait, and H. Funabiki. 2007. Chromosomal enrichment and activation of the aurora B pathway are coupled to spatially regulate spindle assembly. Dev Cell. 12:31-43.

Kollman, J.M., A. Merdes, L. Mourey, and D.A. Agard. 2011. Microtubule nucleation by γ-tubulin complexes. Nat Rev Mol Cell Biol. 12:709-721.

Kolmogorov, A., and I. Petrovskii. 1937. A study of the diffusion equation with a source term for application to a biological problem. Bull. Moscow State Univ. A.

Loose, M., E. Fischer-Friedrich, J. Ries, and K. Kruse. 2008. Spatial regulators for bacterial cell division self-organize into surface waves in vitro. Science.

Loose, M., K. Kruse, and P. schwille. 2011. Protein Self-Organization: Lessons from the Min System. Biophysics.

Luther, R. 1987. Propagation of chemical reactions in space. Journal of Chem. Edu. 64:740.

Mandelkow, E.M., and E. Mandelkow. 1992. Microtubule oscillations. Cell Motil. Cytoskeleton. 22:235-244.

Masui, Y. 1972. Distribution of the cytoplasmic activity inducing germinal vesicle breakdown in frog oocytes. J. Exp. Zool.

Meng, W., Y. Mushika, T. Ichii, and M. Takeichi. 2008. Anchorage of microtubule minus ends to adherens junctions regulates epithelial cell-cell contacts. Cell. 135:948-959.

Méndez, V., S. Fedotov, and W. Horsthemke. 2010. Reaction-Transport Systems. Springer. 1 pp.

Mitchison, T., and M. Kirschner. 1984. Dynamic instability of microtubule growth. Nature.

Mitchison, T., M. Wühr, P. Nguyen, K. Ishihara, A. Groen, and C.M. Field. 2012. Growth, interaction, and positioning of microtubule asters in extremely large vertebrate embryo cells. Cytoskeleton. 69:738-750.

Morgan, D.O. 2007. The Cell Cycle: Principles of Control. New Science Press. 1 pp.

Murata, T., S. Sonobe, T.I. Baskin, S. Hyodo, S. Hasezawa, T. Nagata, T. Horio, and M. Hasebe. 2005. Microtubule-dependent microtubule nucleation based on recruitment of gamma-tubulin in higher plants. Nature Cell Biology. 7:961-968.

Murray, J.D. 2002. Mathematical Biology. Springer. 1 pp.

Nakamura, M., D.W. Ehrhardt, and T. Hashimoto. 2010. Microtubule and katanin-dependent dynamics of microtubule nucleation complexes in the acentrosomal Arabidopsis cortical array. Nature Cell Biology. 12:1064-1070.

Niethammer, P., I. Kronja, S. Kandels-Lewis, S. Rybina, P. Bastiaens, and E. Karsenti. 2007. Discrete states of a protein interaction network govern interphase and mitotic microtubule dynamics. PLoS Biol. 5:e29.

Novak, B., and J.J. Tyson. 1993. Modeling the Cell Division Cycle: M-phase Trigger, Oscillations, and Size Control. J. Theor. Biol.

Oddoux, S., K.J. Zaal, V. Tate, A. Kenea, S.A. Nandkeolyar, E. Reid, W. Liu, and E. Ralston. 2013. Microtubules that form the stationary lattice of muscle fibers are dynamic and nucleated at Golgi elements. The Journal of cell biology. 203:205-213.

Ori-McKenney, K.M., L.Y. Jan, and Y.-N. Jan. 2012. Golgi outposts shape dendrite morphology by functioning as sites of acentrosomal microtubule nucleation in neurons. Neuron. 76:921-930.

Petersen, J., and I.M. Hagan. 2005. Polo kinase links the stress pathway to cell cycle control and tip growth in fission yeast. Nature. 435:507-512.

Petry, S., A.C. Groen, K. Ishihara, T.J. Mitchison, and R.D. Vale. 2013. Branching microtubule nucleation in *Xenopus* egg extracts mediated by augmin and TPX2. Cell. 152:768-777.

Pérez-Mongiovi, D., C. Beckhelling, P. Chang, C.C. Ford, and E. Houliston. 2000. Nuclei and microtubule asters stimulate maturation/M phase promoting factor (MPF) activation in *Xenopus* eggs and egg cytoplasmic extracts. The Journal of cell biology. 150:963-974.

Pérez-Mongiovi, D., P. Chang, and E. Houliston. 1998. A propagated wave of MPF activation accompanies surface contraction waves at first mitosis in *Xenopus*. J Cell Sci. 111 (Pt 3):385-393.

Picard, A., E. Karsenti, M.C. Dabauvalle, and M. Dorée. 1987. Release of mature starfish oocytes from interphase arrest by microinjection of human centrosomes. Nature. 327:170-172.

Pines, J., and T. Hunter. 1991. Human cyclins A and B1 are differentially located in the cell and undergo cell cycle-dependent nuclear transport. The Journal of cell biology. 115:1-17.

Rankin, S., and M.W. Kirschner. 1997. The surface contraction waves of *Xenopus* eggs reflect the metachronous cell-cycle state of the cytoplasm. Curr Biol. 7:451-454.

Raskin, D.M., and P.A. de Boer. 1999. Rapid pole-to-pole oscillation of a protein required for directing division to the middle of Escherichia coli. Proceedings of the National Academy of Sciences of the United States of America. 96:4971-4976.

Rivero, S., J. Cardenas, M. Bornens, and R.M. Rios. 2009. Microtubule nucleation at the cis-side of the Golgi apparatus requires AKAP450 and GM130. EMBO J. 28:1016-1028.

Salmon, E.D., W.M. Saxton, R.J. Leslie, M.L. Karow, and J.R. McIntosh. 1984. Diffusion coefficient of fluorescein-labeled tubulin in the cytoplasm of embryonic cells of a sea urchin: video image analysis of fluorescence redistribution after photobleaching. The Journal of cell biology. 99:2157-2164.

Sampath, S.C., R. Ohi, O. Leismann, A. Salic, A. Pozniakovski, and H. Funabiki. 2004. The chromosomal passenger complex is required for chromatin-induced microtubule stabilization and spindle assembly. Cell. 118:187-202.

Studies of nuclear and cytoplasmic behaviour during the five mitotic cycles that precede gastrulation in Drosophila embryogenesis. 1983. Studies of nuclear and cytoplasmic behaviour during the five mitotic cycles that precede gastrulation in Drosophila embryogenesis.

Tabony, J., and D. Job. 1990. Spatial structures in microtubular solutions requiring a sustained energy source. Nature. 346:448-451.

Tischer, T., E. Hörmanseder, and T.U. Mayer. 2012. The APC/C inhibitor XErp1/Emi2 is essential for *Xenopus* early embryonic divisions. Science. 338:520-524.

Tomchik, K.J., and P.N. Devreotes. 1981. Adenosine 3'-5'-monophosphate waves in Dictyostelium discoideum: a demonstration by isotope dilution–fluorography. Science. 212:443-446.

Turing, A.M. 1952. The Chemical Basis of Morphogenesis. Philosophical Transactions of the Royal Society B: Biological Sciences. 237:37-72.

Verde, F., M. Dogterom, E. Stelzer, E. Karsenti, and S. Leibler. 1992. Control of microtubule dynamics and length by cyclin A- and cyclin B-dependent kinases in *Xenopus* egg extracts. The Journal of cell biology. 118:1097-1108.

Vinod, P.K., X. Zhou, T. Zhang, T.U. Mayer, and B. Novak. 2013. The role of APC/C inhibitor Emi2/XErp1 in oscillatory dynamics of early embryonic cell cycles. Biophys Chem. 177-178:1-6.

Wakefield, J.G., J.Y. Huang, and J.W. Raff. 2000. Centrosomes have a role in regulating the destruction of cyclin B in early Drosophila embryos. Curr Biol. 10:1367-1370.

Weiner, O.D., M.C. Rentel, A. Ott, G.E. Brown, M. Jedrychowski, M.B. Yaffe, S.P. Gygi, L.C. Cantley, H.R. Bourne, and M.W. Kirschner. 2006. Hem-1 Complexes Are Essential for Rac Activation, Actin Polymerization, and Myosin Regulation during Neutrophil Chemotaxis. PLoS Biol. 4:e38.

Weiner, O.D., W.A. Marganski, L.F. Wu, S.J. Altschuler, and M.W. Kirschner. 2007. An Actin-Based Wave Generator Organizes Cell Motility. PLoS Biol. 5:e221.

Whitaker, M. 2006. Calcium at fertilization and in early development. Physiol. Rev. 86:25-88.

Wiese, C., and Y. Zheng. 2006. Microtubule nucleation: gamma-tubulin and beyond. J Cell Sci. 119:4143-4153.

Wilson, E.B. 1896. The Cell in development and inheritance. Macmillan, New York. 1 pp.

Wühr, M., E.S. Tan, S.K. Parker, H.W. Detrich, and T.J. Mitchison. 2010. A model for cleavage plane determination in early amphibian and fish embryos. Curr Biol. 20:2040-2045.

Wühr, M., N.D. Obholzer, S.G. Megason, H.W. Detrich, and T.J. Mitchison. 2011. Live imaging of the cytoskeleton in early cleavage-stage zebrafish embryos. Methods in Cell Biology: Volume 95. 101:1-18.

Wühr, M., S. Dumont, A.C. Groen, D.J. Needleman, and T.J. Mitchison. 2009. How does a millimeter-sized cell find its center? Cell Cycle. 8:1115-1121.

Wühr, M., Y. Chen, S. Dumont, A.C. Groen, D.J. Needleman, A. Salic, and T.J. Mitchison. 2008. Evidence for an upper limit to mitotic spindle length. Curr Biol. 18:1256-1261.

Yoneda, M., Y. Kobayakawa, H.Y. Kubota, and M. Sakai. 1982. Surface contraction waves in amphibian eggs. J Cell Sci. 54:35-46.

Zhabotinsky, A.M. 1991. A history of chemical oscillations and waves. Chaos. 1:379-386.

We must therefore ascribe to living cells, beyond the molecular structure of the organic compounds that they contain, still another structure of different type of complication; and it is this which we call by the name of organization.

Ernst von Brücke

2

Microtubule nucleation during aster growth

Abstract

A major challenge in cell biology is to understand how nanometer sized molecules can organize micron-sized cells in space and time. One solution in many animal cells is a radial array of microtubules called an aster, which is nucleated by a central organizing center and spans the entire cytoplasm. Frog (here *Xenopus laevis*) embryos are more than one millimeter in diameter and divide with a defined geometry every 30 minutes. Like smaller cells, they are organized by asters, which grow, interact and move to precisely position the cleavage planes. It has been unclear whether asters grow to fill the enormous egg by the same mechanism used in smaller somatic cells, or if special mechanisms are required. We addressed this question by imaging growing asters in a cell-free system derived from eggs, where asters grew to hundreds of microns in diameter. By tracking marks on the lattice, we found that microtubules could slide outward, but this was not essential for rapid aster growth. Polymer treadmilling did not occur. By measuring the number and positions of microtubule ends over time, we found that most microtubules were nucleated away from the centrosome, and that interphase egg cytoplasm supported spontaneous nucleation after a time lag. We propose that aster growth is initiated by centrosomes, but that asters grow by propagating a wave of microtubule nucleation stimulated by the presence of pre-existing microtubules.

2.1 INTRODUCTION

The large cells in early vertebrate embryos are organized by radial arrays of microtubules called asters. This general organization was described by early cytologists (Wilson, 1925), but is clearly illustrated by modern fixed immunofluorescence or live imaging. At the end of mitosis, a pair of asters is observed at the spindle poles but remain small in radius, presumably because Cdk1 inhibits aster growth (Wühr et al., 2008). Once the cell enters interphase, the asters grow at rates of 30 μm/min in *Xenopus* zygotes and 15 μm/min in zebrafish, while maintaining a high density of microtubules at their periphery (Wühr et al., 2008; 2010; 2009). Paired asters interact at the cell's midplane to form a specialized zone of microtubule overlaps, which in turn recruit cytokinesis factors to the cell cortex (Nguyen et al., 2014; Mitchison et al., 2012). Cell-spanning dimensions are presumably required so that the microtubules can touch the cortex to accurately position the cleavage furrow according to cell geometry (Rappaport, 1996; Wühr et al., 2010; Minc et al., 2011).

In the standard model of aster growth, microtubules are nucleated with their minus-ends anchored at the centrosome (Brinkley, 1985) and polymerize outward with plus-ends undergoing dynamic instability (Mitchison and Kirschner, 1984). However, there are several issues in applying this model to a very large cytoplasm (Ishihara et al., 2014). Due to the radial geometry, the standard model implies a decrease in microtubule density with increasing radius. In contrast, microtubule density appears to be constant or even increase towards the aster periphery in frog and fish zygotes (Wühr et al., 2010). Furthermore, this radial elongation model predicts that a subset of microtubules spans the entire aster radius, but it is unknown if such long microtubules exist. We wondered if additional mechanisms promoted aster growth in large cells, such as microtubule sliding, treadmilling or nucleation remote from centrosomes.

Previously, we developed a cell-free system to reconstitute cleavage furrow signaling where growing asters interacted (Nguyen et al., 2014; Field et al., 2014). Here, we combine cell-free reconstitu-

tion and quantitative imaging to identify microtubule nucleation away from the centrosome as the key biophysical mechanism underlying aster growth. We propose that aster growth in large cells should be understood as a spatial propagation of microtubule-stimulated microtubule nucleation.

2.2   Results

2.2.1   Reconstitution of large asters in a cell-free system

To study aster growth, we used extracts made from unfertilized frog eggs (Murray, 1991) and added calcium immediately before imaging to initiate the interphase cell cycle (Field et al., 2014). These extracts are essentially undiluted cytoplasm and support the growth and interaction of large asters that reconstitute spatially organized signaling characteristic of cytokinesis in zygotes (Figure 2.1A and Nguyen et al., 2014). In most experiments, asters were nucleated with beads coated with activating antibody to Aurora kinase A (AurkA) (Tsai and Zheng, 2005). This kinase plays a key role in microtubule nucleation. The beads mimic centrosomes and lead to similar aster growth as the physiological nucleation site, a pair of centrosomes attached to sperm chromatin (Figure B.1A). However, unlike demembranated sperm, the beads provide a point-like center to the aster and facilitate image analysis by avoiding chromatin-mediated nucleation and splitting of the centrosome pair.

At higher bead densities, asters interact, which mutually inhibit further growth (Figure 2.1A and Nguyen et al., 2014). At low bead density, we observed assembly of asters as large as those observed in vivo, spanning 500 μm or more in radius (Figure 2.1B and C). Aster radius grew continuously for 30-80 minutes after addition of calcium. At later time points, microtubules often appeared spontaneously in the cytoplasm, which interfered with further aster growth (Figure B.1B). The centers of asters in extract usually did not show a drastic loss of microtubules as seen in fixed frog zygotes or live zebrafish embryos (Wühr et al., 2010). We concluded that our cell-free system was capable of reconstituting large asters at length and time scales of aster growth similar to those in frog zygotes,
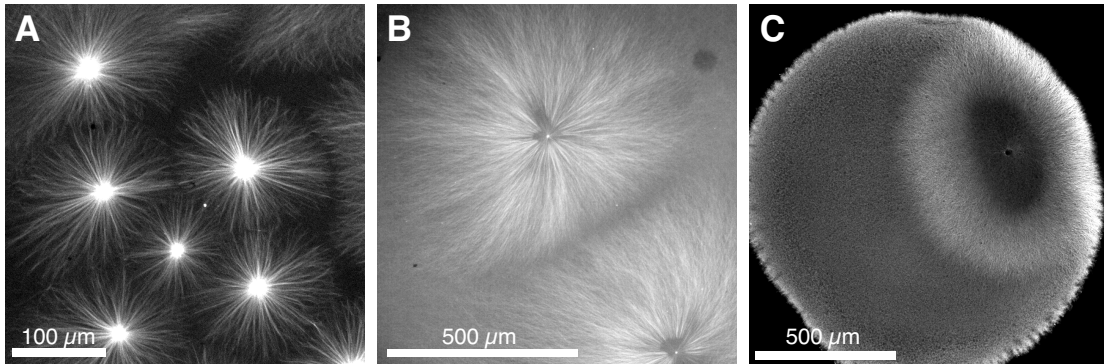
Figure 2.1: **Reconstitution of large microtubule asters in a cell-free system.** (A) High density of beads coated with Aurora kinase A (AurkA) antibody in interphase *Xenopus* egg extract nucleate many asters that mutually inhibit their growth upon contact, leading to limited radii. 34 min post calcium addition. Scale bar 100 µm. (B) At low bead densities, asters are spatially separated and grow in an uninterrupted manner. Large asters spanning 500 µm in radius are observed. 45 min post calcium addition. Scale bar 500 µm. Widefield images of fluorescently labeled tubulin. (C) Asters grow and eventually span the entire cytoplasm of *Xenopus laevis* zygote. Laser scanning confocal images of eggs fixed at 45 min post fertilization and stained for tubulin by immunofluorescence. Scale bar 500 µm.

and decided to use this system to study aster growth mechanisms.

2.2.2 LARGE ASTERS ASSEMBLE IN THE ABSENCE OF MICROTUBULE SLIDING

One biophysical process that might contribute to aster growth is outward microtubule sliding (Wühr et al., 2009; Waterman-Storer et al., 2000). To assess this, we applied fluorescent speckle microscopy (Danuser and Waterman-Storer, 2006). Speckles result from random incorporation of a small fraction of labeled tubulin into the microtubule lattice, and can be used as fiduciary marks to detect polymer sliding. Speckle movement was quantified using velocimetry software (see methods). To illustrate sliding movement we also show kymographs in Figure 2.2. Asters assembled on uncoated glass coverslips exhibited highly curved and disorganized microtubules at their periphery (Figure 2.2A), and the microtubules slid radially outward at 6.1 ± 2.8 µm/min (standard deviation SD, n = 12 asters) (Figure 2.2B and Movie B.1).

Outward sliding is likely driven by dynein pulling from sites in the cytoplasm and/or coverslip surface (Waterman-Storer et al., 2000). One candidate is the minus-end directed motor dynein.

uncoated surface   uncoated surface + dynein inhibition   PLL-PEG surface

interior → periphery

60 s
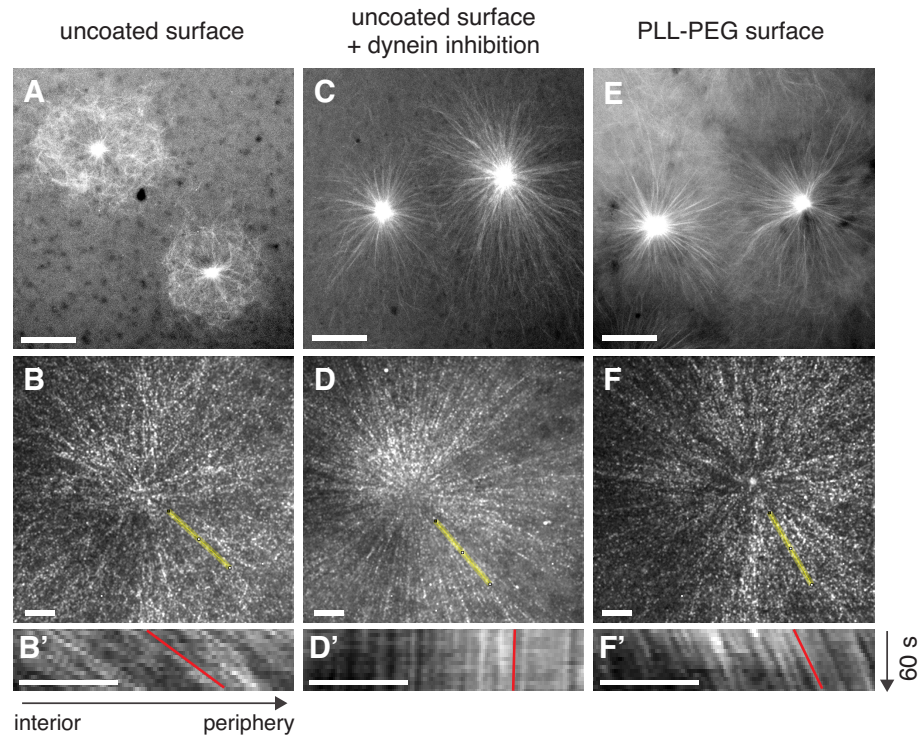
Figure 2.2: **Large asters assemble in the absence of dynein-mediated microtubule outward sliding.** (A) Asters assembled between uncoated coverslips show curved and disorganized microtubules. Image acquired on a widefield microscope. 15 min post calcium addition. Scale bar 50 μm. (B) First frame of a fluorescence speckle microscopy movie showing labeled tubulin in an aster near its center. Image acquired on a spinning disc microscope. See Movie B.1. Movies were subjected to particle image velocimetry to determine the outward sliding rate as 6.08 ± 2.76 μm/min (standard deviation, n = 12 asters). Scale bar 10 μm. (B') Kymographs generated from yellow line in B, where left to right corresponds to interior to periphery of the aster. Scale bar 10 μm. (C-D') Same as A-B', in the presence of p150-CC1 protein to inhibit dynein motor activity. Note the decreased curving of aster microtubules and the complete suppression of microtubule outward sliding, -0.16 ± 0.25 μm/min (n = 12 asters). See Movie B.2. (E-F') Same as A-B', with the coverslip surface passivated by poly-L-lysine-PEG (PLL-PEG). This also resulted in the decrease of microtubule curving and the reduction of microtubule outward sliding to 2.70 ± 1.16 μm/min (n = 6 asters). See Movie B.3.

When dynein was inhibited by addition of the p150-CC1 fragment of dynactin (King et al., 2003), still on uncoated glass coverslips, microtubules were much more straight and bundled (Figure 2.2C) and outward sliding was blocked (Figure 2.2D and Movie B.2). Thus, both curving and outward sliding were driven by dynein. Passivating the coverslip surface by adsorption of poly-L-lysine PEG (PLL-PEG) also resulted in loss of most curling (Figure 2.2E), and decreased outward sliding rate to 2.7 ± 1.2 μm/min (SD, n = 6 asters) (Figure 2.2F and Movie B.3). Presumably, surface passivation by PLL-PEG decreased dynein binding to the glass, and this decreased its sliding and curling actions. Despite the varying degrees of microtubule sliding, we observed large asters spanning hundreds of microns in all conditions. In a previous study in zebrafish embryos, dynein perturbation inhibited aster movement but not their growth (Wühr et al., 2010). Taken together, we conclude that outward microtubule sliding can occur in growing asters, and might contribute to growth in eggs, but is not essential for growth. The effect of microtubule sliding on aster growth rate is discussed below.

2.2.3 Microtubule treadmilling does not occur during aster growth

Another process that could contribute to aster expansion, which speckle microscopy would miss, is outward treadmilling. Polymer treadmilling occurs when one end of a microtubule polymerizes while the other depolymerizes. This would have an effect of increasing microtubule density at the periphery while decreasing it in the interior of the aster. Given the orientation of microtubules in the aster, we would expect outward plus-end polymerization and outward minus-end depolymerization as evidence of treadmilling.

To test this prediction, we performed intensity difference analysis between subsequent frames in tubulin images collected by TIRF microscopy (Figure 2.3A, Movie B.4). We inhibited microtubule sliding via dynein inhibition and focused on the interior of established asters, where movement of microtubules normal to their axis was minimal. In the images that represent the positive difference between subsequent frames, we observed polymerization (Figure 2.3A, top right and Movie B.5).

43
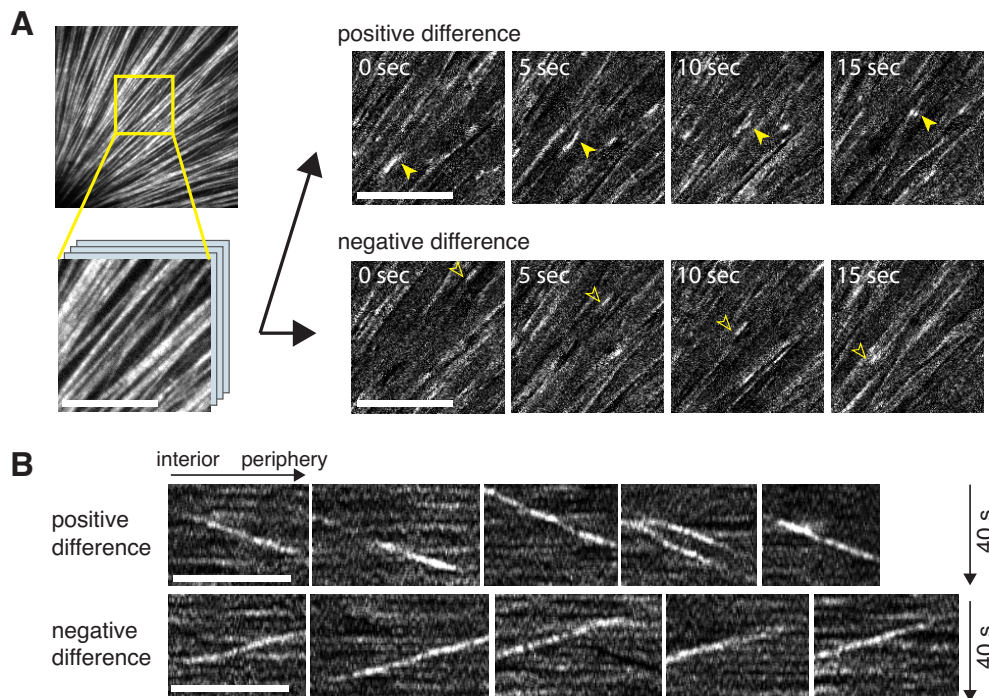
Figure 2.3: **Tubulin intensity difference imaging reveals dynamic microtubule plus-ends in a growing aster.** (A) Microtubules were imaged with labeled tubulin by TIRF microscopy (see Movie B.4). To facilitate analysis of polymer dynamics, intensity differences of subsequent images were calculated to yield maps of polymerization (positive difference, Movie B.5) and depolymerization (negative difference, Movie B.6). See methods. Scale bar 10 μm. (B) Kymographs were constructed to measure the rates of polymerization and depolymerization observed above. Polymerization proceeded outward at 30.0 ± 4.3 μm/min (standard deviation, n = 56 ends from 4 asters) while depolymerization traveled inward at 41.8 ± 5.2 μm/min (standard deviation, n = 50 ends from 4 asters) representing plus-end dynamics. Scale bar 10 μm.

This morphologically resembled EB1-GFP comets (see below) consistent with a spatial map of microtubule polymerization at their plus-ends. Kymograph analysis suggested outward polymerization rates of 30.0 ± 4.3 μm/min (SD, n = 56 ends from 4 asters) (Figure 2.3B, top), in agreement with similarly analyzed EB1 comet velocities 28.2 ± 2.8 μm (SD, n = 32 ends). In the images that represent negative difference, we observed shrinkage of microtubules. Here, we observed rapid inwards movement at 41.8 ± 5.2 μm/min (SD, n = 50 ends from 4 asters) (Figure 2.3A, bottom right and Movie B.6), presumably corresponding to plus-end depolymerization (Figure 2.3B, bottom). We did not

observe outward depolymerization of minus-ends, which would have been the signature of outward treadmilling. In summary, this analysis was most consistent with aster microtubules undergoing classic, two-state dynamic instability on plus-ends, and no fast polymerization dynamics on minus-ends.

2.2.4 Quantification of plus-end density and aster growth rate

To measure the spatiotemporal distribution of microtubule plus-ends during aster growth, we added EB1-GFP, a microtubule associated protein that tracks growing plus-ends as bright comets (Tirnauer et al., 2002), and quantified them by image analysis. Every 2 min, a single image of labeled tubulin was acquired, followed by four images of EB1-GFP at 3-second intervals (Figure 2.4A). An automated image analysis procedure (Applegate et al., 2011) tracked plus-end growth rate and direction, and most important for this study, counted the number of EB1 comets found at a given distance from the center of the aster. In this way, we obtained a quantitative description of aster growth in terms of total EB1 comet number (Figure 2.4B) and density (Figure 2.4C). Compared to tubulin fluorescence intensity, which suffers from low signal-to-noise, EB1 counting is a sensitive method for detecting microtubules (see Figure 2.4A insets). We determined the aster edge as the half-max position of the EB1 comet distribution curves (Figure 2.4B) at different time points. This analysis showed that aster radius increased linearly at a constant rate (Figure 2.4B inset). We quantified the growth rate of aster radius as 29.0 ± 2.9 μm/min (SD, n = 5 asters) in the presence of dynein-mediated microtubule outward sliding (EB1 density plots in Figure B.2A) and 22.0 ± 4.1 μm/min (SD, n = 9 asters) with dynein inhibition. As expected, dynein-mediated outward sliding of microtubules accelerated aster growth rate (Figure B.2B). These radial expansion rates are comparable to the estimated 25-30 μm/min aster growth rates in frog embryos (Wühr et al., 2010).

45

In the radial elongation model with constant microtubule nucleation from the centrosome, we would expect a spatial dilution of EB1 comets with increasing distance from the center. However, an increasing number of EB1 comets appear with aster growth (Figure 2.4B) and the comet density was fairly uniform away from the AurkA bead at 0.03-0.04 per μm2 (Figure 2.4C). The focal plane with a 20x 0.75NA objective is 2 μm deep in z, and most EB1 comets were concentrated at a single focal plane using PLL-PEG passivated coverslips. Assuming a sample thickness of 10 μm, we can extrapolate a volume density of 0.006-0.008 growing plus-ends per μm3, but this value is only an estimate. Our quantitative measurements of reconstituted asters show that microtubules are not spatially diluted in the radial geometry and strongly suggest that new microtubule ends are generated in the aster at locations far away from the organizing center.

2.2.5 Plus-ends are generated at locations far from AurkA beads during aster growth

To estimate what fraction of the microtubules in an aster originate from our centrosome mimic, the AurkA beads, we counted the number of tracks that crossed a circle of radius 40 μm away from the bead (Figure 2.5A) where EB1 comets stayed in a single focal plane, allowing for reliable tracking (Figure 2.5A'). This radius was chosen arbitrarily, but the analysis is not very sensitive to it (Figure 2.5B). We estimated the nucleation rate from AurkA beads as 62 ± 17 microtubules per min (SD, n = 8 time points) in an imaged quadrant, or 250 per min in the whole aster. This rate stayed constant over 30 min in some asters (Figure 2.5B) and extract preparations, while in others, the rate gradually decreased, and the center of the aster slowly hollowed out. The EB1 comet densities of examples with and without hollowing are shown in Figure 2.4D. Figure 2.5B shows nucleation rate from the AurkA bead over time, determined as Figure 2.5A', which was fairly constant in this example. Figure 2.5C shows total EB1 comet number over time in the whole quadrant (blue circles) and the time-integrated contribution from bead nucleation (red crosses). Comparison of these two plots reveals

Figure 2.4 *(following page)*: **Quantification of microtubule plus-ends during aster growth.** (A) Live imaging of labeled tubulin and the plus-end tracking protein EB1-GFP using widefield microscopy. Images show dynein inhibited asters assembled under PLL-PEG passivated coverslips. Inset shows magnification of region in yellow box. Time indicates time post calcium addition. Scale bar 100 μm. (B) Time evolution of the number of EB1 comets detected at a given distance. Comets were detected and tracked using the PlusTipTracker software (Applegate et al., 2011, see methods). Inset shows half-max positions of the EB1 comet number at different time points. (C) Time evolution of the EB1 comet density at a given distance. (D) Gallery showing the EB1 density of multiple examples of aster growth. Curves in each plot are 2 min apart.
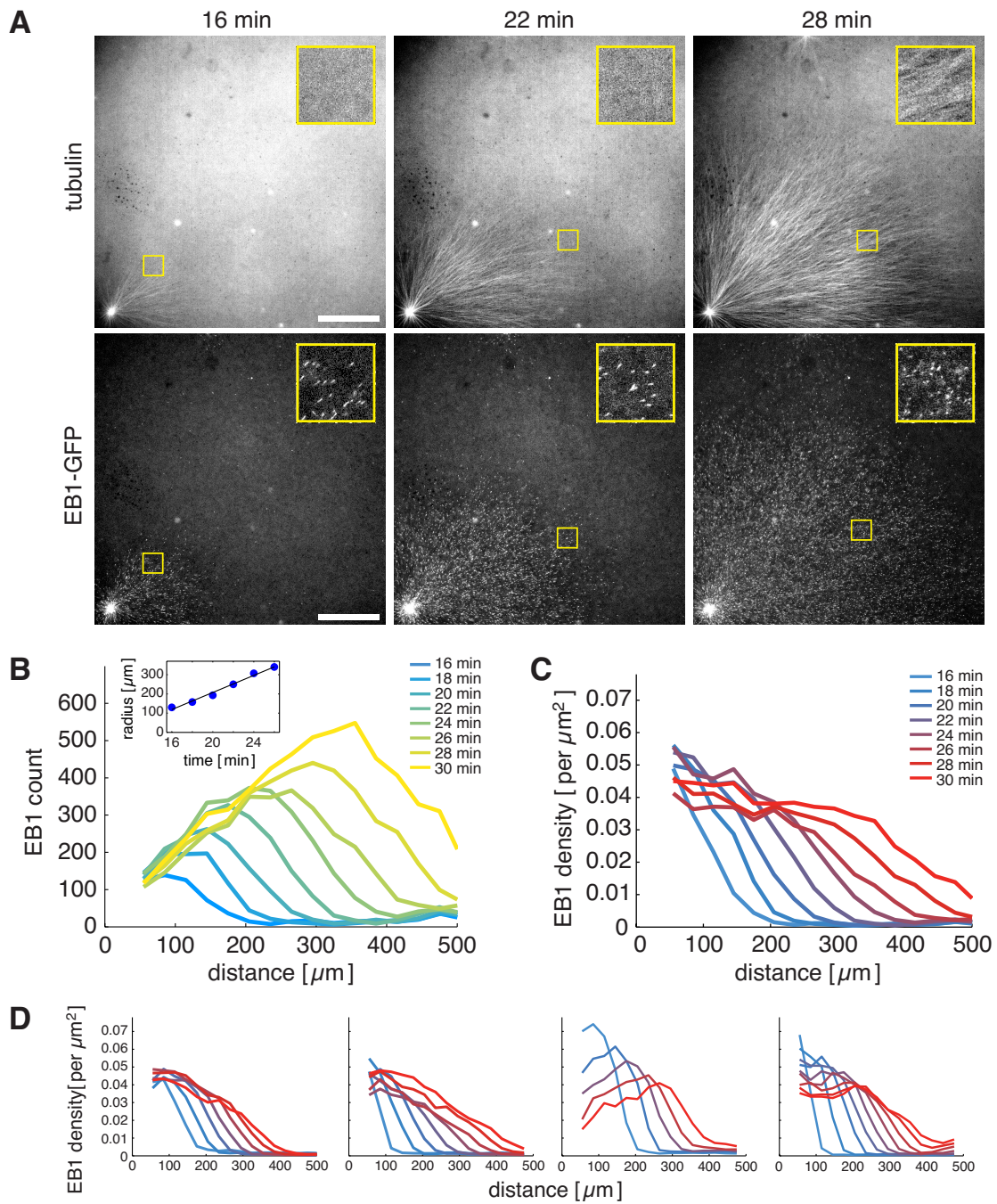
that the fraction of total growing plus-ends within an aster due to nucleation from the bead decreases over time, as nucleation away from the bead starts to dominate (Figure 2.5D inset). Analysis of multiple asters (Figure B.3) led us to conclude that that our centrosome mimic, the AurkA bead, contributes at most 50% of plus-ends to the entire aster during growth, and often far less.

2.2.6 Microtubule nucleation and aster assembly in the absence of centrosomes

Our quantitative analysis pointed to a centrosome-independent origin of microtubule ends during aster growth. To directly test the requirement of centrosomes for microtubule nucleation, we imaged interphase extract in the absence of added nucleating templates. Initially, EB1 comets were only sparsely observed in the imaging field, but their number started to increase and quickly reached a saturating density of 0.036 per µm2 (Figure 2.6A and B), comparable to the density inside growing asters. The exact timing of spontaneous microtubule assembly was variable, ranging from 20-80 min post calcium addition, and seemed to depend on extract preparation, time elapsed since preparation, and position imaged within the sandwiched extract sample. However, the appearance of EB1 comets consistently exhibited sigmoidal kinetics. We did not observe such rapid microtubule assembly with extracts arrested in meiotic metaphase. Thus, spontaneous microtubule assembly seems to be a property specific to the interphase cytoplasm.

To directly test the requirement of centrosomes in the growth of large asters, we introduced Tetrahymena pellicles in the interphase extract as microtubule nucleation centers. These provide a large number of basal bodies that can elongate microtubules in extract. Pellicles nucleated large asters with radii spanning hundreds of microns that were morphologically similar to asters assembled by sperm and AurkAbeads (Figure 2.6C), except for a higher microtubule density in the center. Thus, aster growth does not require a special biochemical activity of centrosomes. Finally, we asked if aster growth occurs in intact frog eggs devoid of centrosomes. To this end, we artificially

49
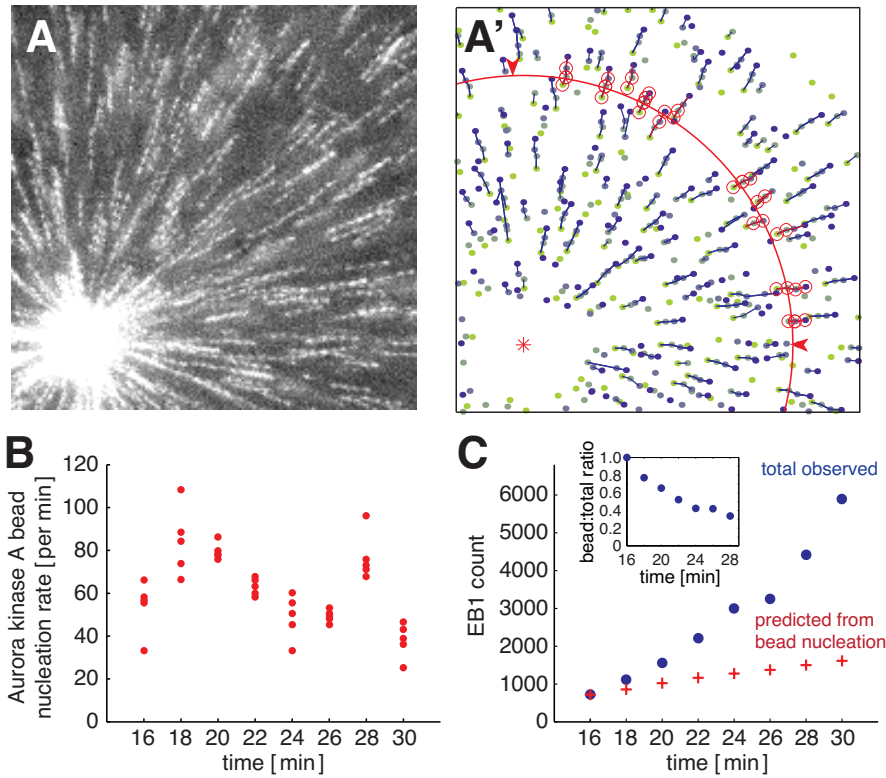
Figure 2.5: **Microtubules in the aster appear at a distance from the organizing center.** (A) Maximum intensity projection of four consecutive EB1-GFP images taken over 9.6 seconds. Same aster as Figure 2.4A at 28 min post calcium addition. (A') Particle tracking was applied to the same four images (shown in A) to measure microtubule nucleation from AurkA bead (red asterisk). All EB1 comets detected are represented as dots varying from green to blue (frame 1 to 4). Blue lines represent all detected tracks. Red circles indicate tracks that were detected as crossing the 40 µm perimeter (line). See methods for details. (B) AurkA bead nucleation rate measure as in A'. For each time point, number of comets crossing over radii of 38, 39, 40, 41, 42 µm are shown in the plot. (C) Total number of EB1 comets increase dramatically as the aster grows (blue dots). The predicted number of EB1 comets based on the nucleation of AurkA bead alone (red plus signs) is significantly lower. Inset shows the ratio of bead (red) : total (blue) at each time point.
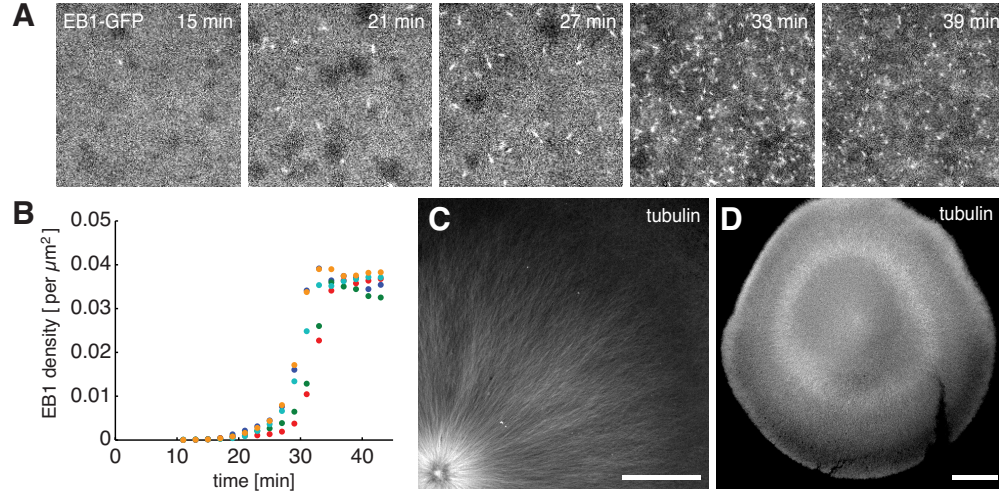
Figure 2.6: **Microtubules assemble in the interphase cytoplasm in the absence of centrosomes.** (A) Timelapse image of spontaneously nucleated microtubules in the interphase extract with EB1-GFP. Time denotes time post calcium addition. Scale bar 10 μm. (B) Quantification of EB1 comet density over time for the same reaction in A. Different colors represent different positions of the same coverslip. (C) Tetrahymena pellicles in interphase extract nucleate microtubules and form large radial arrays of microtubules resembling asters. Scale bar 100 μm. (D) Immunofluorescence image showing the pattern of tubulin in eggs fixed at 90 min post electroactivation. Scale bar 200 μm.

induced eggs to enter the interphase cell cycle by electric shock, fixed and stained for microtubules for immunofluorescence. We observed microtubule patterns resembling asters in some activated eggs (Figure 2.6D) in agreement with previous reports (Elinson and Rowning, 1988; Houliston and Elinson, 1991). Thus, even in the absence of centrosomes, microtubule asters form and span the large interphase cytoplasm of frog eggs.

2.3 DISCUSSION

In this study, we set out to elucidate the biophysical mechanisms underlying the growth of large microtubule asters in large embryonic cells. We first showed that microtubule sliding (Figure 2.2) and treadmilling (Figure 2.3) are not essential to this process, though dynein-driven outward sliding can contribute to the radial expansion rate (Figure B.2). By developing an assay for the quantification of growing plus-end number (Figure 2.4) and nucleation rate from the organizing center (Figure

2.5), we have provided the first definitive evidence for the generation of new microtubule plus-ends away from the centrosome during aster growth. Importantly, new microtubule ends were preferentially generated within growing asters, but they eventually assembled even in the absence of nucleating templates (Figure 2.6). Three distinct mechanisms might explain preferential nucleation within growing asters: (i) a microtubule-independent signal originating from the centrosome and propagating through the cytoplasm which in turn locally instructs microtubule nucleation; (ii) severing of pre-existing microtubules in the aster; (iii) microtubule-stimulated microtubule nucleation occurring in the aster. Mechanism (i) seems unlikely as we found large asters to assemble in interphase extract supplemented with pellicles and in electro-activated eggs lacking centrosomes (Figure 2.6C and D). Mechanism (ii) was not supported by any imaging data, and Katanin, the dominant microtubule-severing enzyme in *Xenopus* egg extract, is known to be inactive in interphase (Vale, 1991; McNally and Vale, 1993). The sigmoidal kinetics of spontaneous microtubule assembly (Figure 2.6B) is consistent with microtubule self-amplification, though other mechanisms could also explain this observation, such as a time-dependent decrease in Cdk1 phosphorylation sites (Field et al., 2011; 2014) that eventually allows nucleation. To simultaneously explain our observations of aster growth and spontaneous microtubule assembly, we favor a mechanism where microtubule nucleation is locally promoted by pre-existing microtubules in the aster.

In contrast to mitotic spindles that are limited in size (Wühr et al., 2008), interphase asters appear to grow in an unbounded manner. In the fish and frog zygotes, asters grow continuously until they contact another aster or the cell cortex (Wühr et al., 2010). In the extract system, aster growth is halted by contact with a neighboring aster (Nguyen et al., 2014; Mitchison et al., 2012) or with spontaneous microtubules that appear in the background at later time points (Figure B.1B). It is of interest whether individual microtubules that compose the unbounded aster are themselves bounded or unbounded in length. In theory, this is determined by the precise dynamics of microtubule plus-ends: if the time-weighted average of polymerization and depolymerization is positive (i.e. net

polymerization), microtubules are unbounded in length. If the average is negative, all plus-ends eventually shrink back to their minus-ends (i.e. net depolymerization), and are replaced by newly nucleated ones. Previous work suggested bounded growth in mitosis and unbounded in interphase (Verde et al., 1992). Our EB1 and tubulin images suggest the existence of approximately steady-state conditions for both total microtubule density and total growing plus-end density in the aster interior. This implies that the growth of individual microtubules is bounded, at least in the aster interior. If it was unbounded, either the total microtubule density would have to increase continually, which would be evident in tubulin images, or the plus-end density would have to decrease significantly, which was usually not observed (Figure 2.4D). We propose that individual microtubules are bounded in length but self-amplifying nucleation promotes the aster growth in an unbounded manner to span the millimeter-sized cytoplasm. How microtubule dynamics and nucleation contribute to aster growth rate and microtubule density is an important topic for future studies.

We propose a two-step model of aster growth in large embryonic cells (Figure 2.7). Aster growth is initiated by AurkA-dependent microtubule nucleation at the centrosome, but the length of these microtubules is bounded by the dynamic instability of plus-ends. When sufficient local microtubule density builds up, or perhaps when Cdk1 site phosphorylation drops below some threshold, aster growth transitions to a phase were microtubule-stimulated microtubule nucleation promotes expansion of the aster periphery while maintaining high microtubule density. Local initiation coupled with a signal-amplification mechanism has been highlighted as an important design principle underlying the mitotic trigger waves that coordinate the large cytoplasm of frog eggs (Chang and Ferrell, 2013; Ishihara et al., 2014). Similarly, our model of aster growth views the interphase cytoplasm as an excitable system for microtubule assembly. In contrast to the cell cycle oscillator whose molecular components and dynamics have been well studied, much less is known about microtubule nucleation and how it may be regulated by pre-existing microtubules (Petry et al., 2013; Clausen and Ribbeck, 2007; Murata et al., 2005; Goshima et al., 2008). Studying aster growth as an emergent
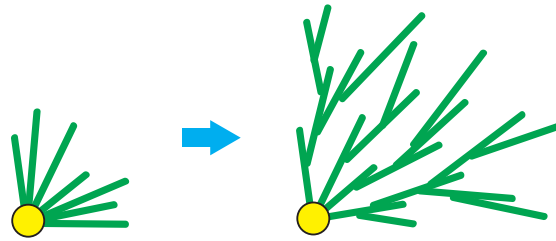
Figure 2.7: **A two-step model for large aster growth.** At early time points, aster growth is initiated by Aurora kinase A-dependent microtubule nucleation at the centrosome. Later in interphase, aster growth is sustained by microtubule nucleation away from the centrosome, presumably stimulated by pre-existing microtubules.

property of microtubules may allow us to address these outstanding issues.

2.4 Materials and Methods

Aster reconstitution in *Xenopus* egg extract

Xenopus egg extract were prepared and interphase asters were assembled using Protein A Dynabeads (Life Technologies) coated with Aurora kinase A antibody as described (Field et al., 2014; Nguyen et al., 2014). Addition of the actin depolymerizing drug cytochalasin D had no noticeable effect on aster growth and the majority of data presented in this study omitted it. EB1-GFP was purified as in (Petry et al., 2011) and used at a final concentration of 60 nM. For dynein inhibition, the p150-CC1 fragment of dynactin was purified as in (King et al., 2003) and used at a final concentration of 0.04 mg/ml. Poly-L-lysine-PEG was synthesized as in (Huang et al., 2001) and adsorbed to glass coverslips (cleaned by sequential sonication in 3M KOH solution and ethanol) during a 15 min incubation as a 0.01 mg/ml solution in 10 mM K-HEPES pH 7.8 buffer. Tetrahymena pellicles were a gift from Jan Brugues (MPI-CBG, Germany).

Fluorescent speckle microscopy and velocimetry

Alexa647-labeled bovine tubulin was used at a final concentration of 5 nM, which corresponds to 1:4000 of tubulin dimers being labeled in the extract. A Nikon E800 upright microscope equipped

with 60x Plan Apo 1.40NA objective lens (Nikon), a Yokogawa CSU10 spinning disc (Perkin Elmer, MA) and a cooled CCD camera (Hamamatsu ORCA-ER), and Melles Griot Krypton/Argon ion laser (488nm, 568nm, 647nm) was driven by Metamorph (Molecular Devices, CA). Aster centers were positioned in the center of the field and images were captured at 4 sec intervals with 2x2 spatial binning mode. Microtubule sliding was quantified using a particle imaging velocimetry plug-in for ImageJ (Tseng et al., 2012). Movement was projected to the radially outward vector and spatially averaged for each movie.

Tubulin intensity difference analysis

Dynein inhibited asters were assembled under coverslips treated with kappa-casein (Field et al., 2014; Nguyen et al., 2014). This passivation reduced surface-binding of unincorporated, labeled tubulin, while still allowing for microtubules to attach to the coverslip. TIRF microscopy was performed on a Nikon Ti-E motorized inverted microscope equipped with a Nikon motorized TIRF illuminator, Perfect Focus, a Prior Proscan II motorized stage, Agilent MLC400B laser launch (488nm, 561nm, 647nm), and an Andor DU-897 EM-CCD camera. Alexa647-labeled bovine tubulin was imaged with a 100x CFI Apo 1.49NA TIRF objective lens (Nikon) coupled with 1.5x tube lens. Stream acquisition of images at 500 ms intervals was performed using the RAM capture mode in NIS-Elements software (Nikon Instruments, Inc.) to yield Movie B.4. ImageJ software (Schneider et al., 2012) was used to construct intensity difference images. As the difference of raw fluorescence intensities was dominated by the gradual photobleaching of the fluorophore, we normalized the signal in each frame prior to image subtraction. The differences of images that were 4 frames apart yielded the best signal to noise ratio. Finally, a rolling average filter of four frames was applied to yield Movie B.5 and B.6. The resultant movies were used to construct kymographs in ImageJ.

Quantification of EB1 comets and aster growth rate

Widefield images were acquired on a Nikon Eclipse Ni-E upright microscope at MBL equipped with a CFI Plan Apochromat Lambda 20x0.75NA objective lens (Nikon), Nikon motorized XY stage, Nikon HG pre-centered fiber illuminator (Intensilight C-HGFIE), and Hamamatsu ORCA-Flash4.0 LT scientific CMOS camera, driven by NIS-Elements. Every 2 min, a single image of labeled tubulin was acquired, followed by four images of EB1-GFP at 3 second intervals. EB1 comets were identified using the PlusTipTracker software (Applegate et al., 2011) and their distribution was analyzed with custom code written in Matlab (Mathworks, MA). The aster growth rate was measured by determining the half-max positions of EB1 count as in Figure 2.4B. Identification of EB1 comets in the absence of nucleating sites was done with the MOSAIC plugin (Shivanandan et al., 2013) for ImageJ. Some images were acquired on the same setup where the Andor Neo sCMOS camera was used instead. Images at HMS were acquired on Nikon 90i upright microscope equipped with 20x CFI Plan Apo 0.75NA, a Prior Lumen 200 metal arc lamp, Prior ProScan III motorized XY stage, Hamamatsu ORCA-ER cooled CCD camera, driven by Metamorph.

Measurement of microtubule nucleation from Aurora kinase A beads

The same positional information of EB1 comets identified in the step above was further processed to estimate the nucleation rate from the AurkA beads. We initially found that PlusTipTracker performed poorly in tracking comets with minimal number of frames, but this was overcome by transforming the comet positions from Cartesian to polar coordinates. This transformation adds the prior knowledge that the EB1 comet trajectories are oriented in the radial direction (rather than random) and resulted in successful reconstruction of trajectories (minimum of three EB1 comets) as verified by manual inspection. A custom Matlab script was used to score comets crossing over a given radius from the bead into the quadrant of interest.

Immunofluorescence imaging of frog eggs

Fertilized eggs were fixed by transfer to 90% Methanol, 50 mM EGTA, processed and stained as described (Nguyen et al., 2014). Samples were imaged with a laser scanning confocal microscope from the Nikon Imaging Center at HMS. Plan Apo 10x 0.45NA (Nikon) and Plan Fluor 20x 0.75NA (Nikon, with Nikon immersion oil) objective lenses were used on a Nikon Ti-E inverted microscope with a Nikon A1R point scanning confocal head, driven by NIS-Elements. For electrical activation, eggs were squeezed into 1x MMR. The jelly coat was removed by swirling the eggs for approximately 5 min in 2% (w/v) cysteine in 0.2x MMR, pH adjusted to 7.8 with KOH, and then rinsing 3x in 0.2x MMR. A horizontal DNA gel box with a bed measuring 8.5 inches from electrode to electrode was filled with 0.2x MMR. De-jellied eggs were placed in a line across the gel box approximately equidistance from both electrodes and shocked with 90 volts DC for 1 second. Pigment contraction at the animal pole a few min after electrical shock indicated successful activation. Eggs were incubated in 0.2x MMR for 40-90 min at 20 C until fixation. Eggs were fixed and imaged as described above.

References

Applegate, K.T., S. Besson, A. Matov, M.H. Bagonis, K. Jaqaman, and G. Danuser. 2011. plusTip-Tracker: Quantitative image analysis software for the measurement of microtubule dynamics. J. Struct. Biol. 176:168-184.

Brinkley, B.R. 1985. Microtubule organizing centers. Annu. Rev. Cell Biol. 1:145-172.

Chang, J.B., and J.E. Ferrell. 2013. Mitotic trigger waves and the spatial coordination of the *Xenopus* cell cycle. Nature. 500:603-607.

Clausen, T., and K. Ribbeck. 2007. Self-organization of anastral spindles by synergy of dynamic instability, autocatalytic microtubule production, and a spatial signaling gradient. PLoS ONE. 2:e244.

Danuser, G., and C.M. Waterman-Storer. 2006. Quantitative Fluorescent Speckle Microscopy of Cytoskeleton Dynamics. Annu. Rev. Biophys. Biomol. Struct. 35:361-387.

Elinson, R.P., and B. Rowning. 1988. A transient array of parallel microtubules in frog eggs: potential tracks for a cytoplasmic rotation that specifies the dorso-ventral axis. Dev Biol. 128:185-197.

Field, C.M., M. Wühr, G.A. Anderson, H.Y. Kueh, D. Strickland, and T.J. Mitchison. 2011. Actin behavior in bulk cytoplasm is cell cycle regulated in early vertebrate embryos. J Cell Sci. 124:2086-2095.

Field, C.M., P.A. Nguyen, K. Ishihara, A.C. Groen, and T.J. Mitchison. 2014. *Xenopus* egg cytoplasm with intact actin. Meth. Enzymol. 540:399-415.

Goshima, G., M. Mayer, and N. Zhang. 2008. Augmin: a protein complex required for centrosome-independent microtubule generation within the spindle. The Journal of cell biology.

Houliston, E., and R.P. Elinson. 1991. Patterns of microtubule polymerization relating to cortical rotation in *Xenopus laevis* eggs. Development. 112:107-117.

Huang, N.P., R. Michel, J. Voros, M. Textor, and R. Hofer. 2001. Poly(l-lysine)-g-poly(ethylene glycol) Layers on Metal Oxide Surfaces: Surface-Analytical Characterization and Resistance to Serum and Fibrinogen Adsorption - Langmuir (ACS Publications). Langmuir.

Ishihara, K., P.A. Nguyen, M. Wühr, A.C. Groen, C.M. Field, and T.J. Mitchison. 2014. Organization of early frog embryos by chemical waves emanating from centrosomes. Philosophical Transac-

tions of the Royal Society B: Biological Sciences. 369.

King, S.J., C.L. Brown, K.C. Maier, N.J. Quintyne, and T.A. Schroer. 2003. Analysis of the dynein-dynactin interaction in vitro and in vivo. Mol Biol Cell. 14:5089-5097.

McNally, F.J., and R.D. Vale. 1993. Identification of katanin, an ATPase that severs and disassembles stable microtubules. Cell. 75:419-429.

Minc, N., D. Burgess, and F. Chang. 2011. Influence of cell geometry on division-plane positioning. Cell. 144:414-426.

Mitchison, T., and M. Kirschner. 1984. Dynamic instability of microtubule growth. Nature.

Mitchison, T., M. Wühr, P. Nguyen, K. Ishihara, A. Groen, and C.M. Field. 2012. Growth, interaction, and positioning of microtubule asters in extremely large vertebrate embryo cells. Cytoskeleton. 69:738-750.

Murata, T., S. Sonobe, T.I. Baskin, S. Hyodo, S. Hasezawa, T. Nagata, T. Horio, and M. Hasebe. 2005. Microtubule-dependent microtubule nucleation based on recruitment of gamma-tubulin in higher plants. Nature Cell Biology. 7:961-968.

Murray, A.W. 1991. Cell cycle extracts. Methods in Cell Biology: Volume 95. 36:581-605.

Nguyen, P.A., A.C. Groen, M. Loose, K. Ishihara, M. Wühr, C.M. Field, and T.J. Mitchison. 2014. Spatial organization of cytokinesis signaling reconstituted in a cell-free system. Science. 346:244-247.

Petry, S., A.C. Groen, K. Ishihara, T.J. Mitchison, and R.D. Vale. 2013. Branching microtubule nucleation in *Xenopus* egg extracts mediated by augmin and TPX2. Cell. 152:768-777.

Petry, S., C. Pugieux, F.J. Nédélec, and R.D. Vale. 2011. Augmin promotes meiotic spindle formation and bipolarity in *Xenopus* egg extracts. Proceedings of the National Academy of Sciences of the United States of America. 108:14473-14478.

Rappaport, R. 1996. Cytokinesis in Animal Cells. Cambridge University Press. 1 pp.

Schneider, C.A., W.S. Rasband, and K.W. Eliceiri. 2012. NIH Image to ImageJ: 25 years of image analysis. Nat. Methods. 9:671-675.

Shivanandan, A., A. Radenovic, and I.F. Sbalzarini. 2013. MosaicIA: an ImageJ/Fiji plugin for spatial pattern and interaction analysis. BMC Bioinformatics. 14:349.

Tirnauer, J.S., S. Grego, E.D. Salmon, and T.J. Mitchison. 2002. EB1-microtubule interactions in *Xenopus* egg extracts: role of EB1 in microtubule stabilization and mechanisms of targeting to microtubules. Mol Biol Cell. 13:3614-3626.

Tsai, M.-Y., and Y. Zheng. 2005. Aurora A kinase-coated beads function as microtubule-organizing centers and enhance RanGTP-induced spindle assembly. Curr Biol. 15:2156-2163.

Tseng, Q., E. Duchemin-Pelletier, A. Deshiere, M. Balland, H. Guillou, O. Filhol, and M. Théry. 2012. Spatial organization of the extracellular matrix regulates cell-cell junction positioning. Proceedings of the National Academy of Sciences of the United States of America. 109:1506-1511.

Vale, R.D. 1991. Severing of stable microtubules by a mitotically activated protein in *Xenopus* egg extracts. Cell. 64:827-839.

Verde, F., M. Dogterom, E. Stelzer, E. Karsenti, and S. Leibler. 1992. Control of microtubule dynamics and length by cyclin A- and cyclin B-dependent kinases in *Xenopus* egg extracts. The Journal of cell biology. 118:1097-1108.

Waterman-Storer, C., D.Y. Duey, K.L. Weber, J. Keech, R.E. Cheney, E.D. Salmon, and W.M. Bement. 2000. Microtubules remodel actomyosin networks in *Xenopus* egg extracts via two mechanisms of F-actin transport. The Journal of cell biology. 150:361-376.

Wilson, E.B. 1896. The Cell in development and inheritance. Macmillan, New York. 1 pp.

Wühr, M., E.S. Tan, S.K. Parker, H.W. Detrich, and T.J. Mitchison. 2010. A model for cleavage plane determination in early amphibian and fish embryos. Curr Biol. 20:2040-2045.

Wühr, M., S. Dumont, A.C. Groen, D.J. Needleman, and T.J. Mitchison. 2009. How does a millimeter-sized cell find its center? Cell Cycle. 8:1115-1121.

Wühr, M., Y. Chen, S. Dumont, A.C. Groen, D.J. Needleman, A. Salic, and T.J. Mitchison. 2008. Evidence for an upper limit to mitotic spindle length. Curr Biol. 18:1256-1261.

What I cannot create, I do not understand.

Richard Feynman

3

A biophysical model for aster growth

Abstract

Microtubule asters - radial arrays of microtubules organized by centrosomes - play a fundamental role in the spatial coordination of animal cells. Asters shape cell morphology, act as tracks for intracellular cargo transport and position the mitotic spindle during cell division. Despite the importance of asters in cell physiology, we lack a biophysical understanding of how asters grow to span the cell. Some of the largest asters are found in fish and amphibian eggs soon after fertilization. In these unusually large, millimeter-sized cells, the radius of the interphase aster increases rapidly without dilution of microtubule density at the periphery. In contrast, mitotic asters remain bounded in radius, making this an ideal system to study how aster size is regulated. Previously, we have suggested that interphase asters grow via microtubule nucleation remote from centrosomes. Here, we present a biophysical model that describes aster growth from microtubule plus end polymerization dynamics and autocatalytic nucleation. This leads us to develop the concept of a critical nucleation rate for aster growth and derive an analytical expression for radial expansion. We propose a scenario where unbounded aster growth consists of individual microtubules that are themselves bounded in length. Thus, large aster growth is an emergent property of dynamic, short microtubules.

3.1 Introduction

Asters, radial arrays of microtubules, are a hallmark of how animal cells spatially organize their cytoplasm (Wilson, 1896). Proper positioning of the nucleus and mitotic spindle rely on molecular motors pulling on astral microtubules (Grill and Hyman, 2005; Neumüller and Knoblich, 2009). Radial interphase microtubules allow efficient formation of ER membrane networks (Waterman-Storer and Salmon, 1998; Wang et al., 2013; Grigoriev et al., 2008). Astral microtubules support cell motility by mediating mechanical and biochemical signals (Etienne-Manneville, 2013). Asters dynamically adapt to cell geometry through the constant polymerization, depolymerization, rearrangement and nucleation of microtubules. How microtubule asters span the cell from the interplay of these processes is a fundamental problem for our understanding of how cells function.

The standard model of aster growth posits that centrosomes nucleate and anchor all microtubules at their minus ends, while their plus ends polymerize via dynamic instability (Brinkley, 1985). However, this textbook model is being increasingly challenged by reports on subpopulations of microtubules with their minus ends located far away from centrosomes. The origin of these non-centrosomal microtubules is not always clear (Keating and Borisy, 1999; Akhmanova and Steinmetz, 2015). Microtubules may become detached from centrosomes and transported outward (Keating et al., 1997; Waterman-Storer et al., 2000). Microtubules may be severed into multiple short pieces (Roll-Mecak and McNally, 2010), or they maybe nucleated in the cytoplasm independent of centrosomes (Efimov et al., 2007; Clausen and Ribbeck, 2007; Petry et al., 2013). While the molecular basis of non-centrosomal microtubules is being investigated, we lack a predictive, mechanistic framework for how these processes might contribute to the overall size and speed of microtubule aster growth.

One particular example of extreme cell size highlights the limitations of the standard model for aster growth. In the early frog and fish embryos, microtubule aster grow to span the enormous, millimeter-sized cytoplasms in a matter of 30 min (Wühr et al., 2008; Mitchison et al., 2012). These

large interphase asters move and center the mitotic spindle (Wühr et al., 2010), and interact with each other to direct the site of cleavage (Wühr et al., 2010; Nguyen et al., 2014). Despite their radial geometry, the density of astral microtubules appears to be constant or increasing with distance from the center (Wühr et al., 2009; Ishihara et al., 2014b). While interphase asters grow continuously until it reaches the cortex, mitotic asters have a small radius and appear to be constant in size. Aster growth and disassembly follows the short cleavage cycles, but the biophysical basis of this reorganization is largely unknown.

We have previously suggested microtubule polymerization dynamics and non-centrosomal nucleation as essential processes for the growth of large interphase asters (Ishihara et al., 2014a). Here, we develop a physical description that accounts for the following two key properties of large aster growth: (i) constant, rapid increase in radius and (ii) lack of microtubule dilution despite the radial geometry. Our theory predicts the quantitative condition for aster growth and the length distribution of microtubules that consist the aster. We propose that unbounded growth of interphase asters is an emergent property of microtubules that are individually bounded in length.

3.2   Physical Description of Asters as Dynamic Microtubule Networks

Biophysical models that capture the collective behavior of cytoskeletal filaments have been proposed to explain the size and shape of intracellular organelles (e.g. the mitotic spindle as in Loughlin et al., 2010 and Brugues and Needleman, 2014) and patterns (e.g. cortical actin waves as in Weiner et al., 2007 and Min waves as in Loose et al., 2011). There exists no quantitative framework that describes the physical basis of microtubule asters. We propose a model of aster growth that focuses on two biophysical processes: (i) polymerization dynamics of individual plus ends and (ii) autocatalytic nucleation of microtubules. Alternative processes such as minus end dynamics, polymer sliding and severing were either non-essential or non-detectable for large interphase asters reconstituted *in vitro* (Ishihara et al., 2014a). The intuition behind our model is to describe aster growth as an

autocatalytic, spatially propagating wave of microtubules initiated by the centrosome (Ishihara et al., 2014b).

3.2.1   Polymerization Dynamics of Individual Microtubules

Microtubules are polar polymers with dynamic plus ends and stable minus ends. To describe the polymerization dynamics of plus ends, we adopt the two-state model of microtubule dynamic instability (Figure 3.1A). In this model, a single microtubule is in either of the two states: (i) the growing state, where plus ends polymerize at rate v_{grow} and (ii) the shrinking state, where plus ends depolymerize at rate v_{shrink}. A growing microtubule may transition to a shrinking one (a catastrophe event) with Poisson arrival rate f_{cat}. Similarly, the shrinking to growing transition (a rescue event) happens at rate f_{res}. We also assume that, when a plus end shrinks back to its minus end, the microtubule disappears. The exception to this is a shrinking microtubule with its minus end anchored to the centrosome, in which case we assume to instantaneously transition to growth.

To understand the implications of the polymerization dynamics, it is instructive to consider the mean polymerization rate J, defined as the time-weighted average of polymerization and depolymerization,

$$\text{mean polymerization rate:} \quad J = \frac{v_g f_{res} - v_s f_{cat}}{f_{res} + f_{cat}}.$$

If $J < 0$, the mean length of a population of microtubules is exponentially distributed with mean length $\langle l \rangle = \frac{-v_g v_s}{v_g f_{res} - v_s f_{cat}}$ (Dogterom and Leibler, 1993; Verde et al., 1992; Bicout, 1997). In the standard model of aster growth, microtubules will be confined to the vicinity of the centrosome and the aster radius will be constant at $\langle l \rangle$. If $J > 0$, the mean microtubule length and the aster radius will increase at velocity J. However, due to the radial geometry, the polymer density will inevitably drop with radial distance (Figure 1B, left). Due to the qualitative change in the mean length of microtubules, these two scenarios have been described as the bounded ($J < 0$) and un-

A polymerization dynamics

v_{growth}

$f_{cat} \updownarrow f_{res}$

v_{shrink}

autocatalytic nucleation

r

B polymerization dynamics only

with nucleation

microtubule density

distance from center (centrosome)
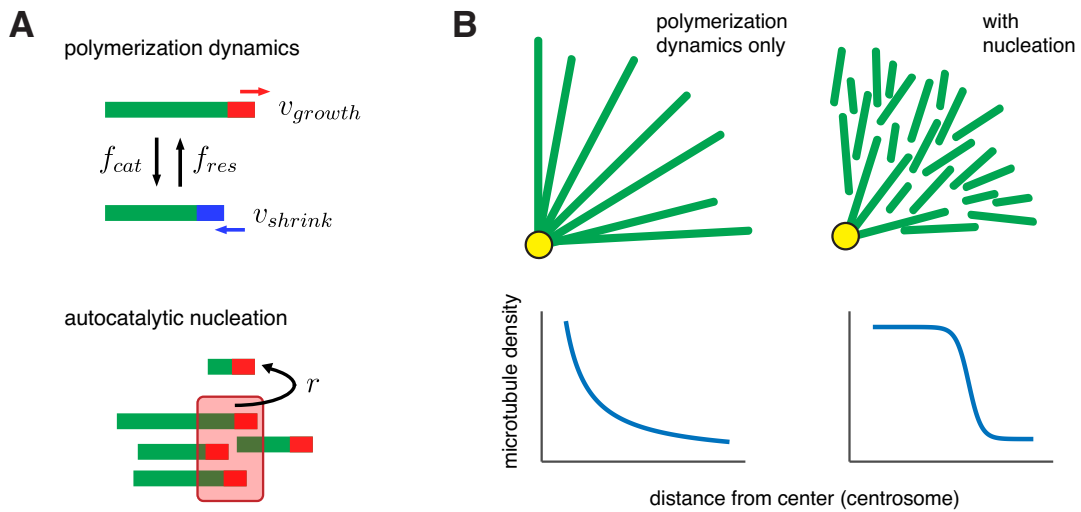
Figure 3.1: **A biophysical model of aster growth.** (A) We describe aster growth from the interplay of two microscopic processes. Individual microtubules undergo two-state plus end dynamic instability with polymerization rate v_{growth}, depolymerization rate v_{shrink}, and transition rates f_{cat} and f_{res}. Autocatalytic microtubule nucleation occurs at rate r catalyzed by the local density of growing plus ends. (B) The model predicts the distribution of microtubules. Polymerization dynamics alone predicts the density of microtubules to drop with distance from the center (centrosome, yellow circle). Addition of autocatalytic nucleation with saturation allows the microtubule density to be kept constant throughout the aster while the aster radius increases.

bounded ($J > 0$) regimes of dynamic instability (Verde et al., 1992; Dogterom and Leibler, 1993). In either case, polymerization dynamics alone cannot explain the observed aster growth that occurs without radial dilution of microtubule density.

3.2.2   AUTOCATALYTIC NUCLEATION OF MICROTUBULES

The process of microtubule nucleation is distinct from polymerization dynamics in that it generates a new pair of plus and minus ends. While the molecular nature of nucleation is not well understood, others have reported autocatalytic kinetics of nucleation (Clausen and Ribbeck, 2007; Petry et al., 2013). For our model of aster growth, we assume (i) nucleation to be the birth of a growing microtubule of zero length, (ii) all microtubules to be oriented with plus ends outward, and (iii) nucleation to be catalyzed by the local density of growing plus ends with the first order rate constant r (Figure 3.1A). The autocatalytic nature of nucleation is at the heart of our model of aster growth as a collective behavior of microtubules.

Autocatalytic processes lead to exponential growth, but physical systems do not permit indefinite growth. Indeed, saturation effects for microtubule nucleation has been observed (Clausen and Ribbeck, 2007; Petry et al., 2013). Possible explanations for such apparent carrying capacity of microtubules in a given volume of cytoplasm include local depletion of starting material (e.g. tubulin), nucleation factors (e.g. gamma-tubulin ring complex and/or its activators), or steric effects. In our model, we impose a carrying capacity volume by expressing autocatalytic nucleation as a logistic function of the local density of growing plus ends. Despite the nucleation rate r being constant in our system, the carrying capacity allows the effect of nucleation to vary in space and time.

We have thus developed a biophysical framework of aster growth that incorporates microtubule plus end polymerization dynamics and autocatalytic nucleation. Autocatalytic nucleation points to the possibility of aster growth where new microtubules are nucleated within the aster and away from the centrosome, compensating for the radial dilution of microtubule density (Figure 1B, right).

The saturation effect ensures that the aster interior is constant in microtubule density. We proceed to analyze if and when such aster growth occurs.

3.2.3   A Continuum Model of Aster Growth

To systematically understand how the interplay of polymerization dynamics and nucleation predict aster growth, we formulate our model into a set of equations assuming continuity (Appendix C). We let $\rho_g(t, x_-, l)$ (or $\rho_s(t, x_-, l)$) denote the number of length $l > 0$, growing (or shrinking) microtubules with their minus ends at distance $x_- > 0$ from the origin. The polymerization dynamics and nucleation is described by the coupled equations,

$$
\begin{cases}
\dfrac{\partial \rho_g}{\partial t} = -v_g \dfrac{\partial \rho_g}{\partial l} - f_{cat}\rho_g + f_{res}\rho_s + Q \cdot \delta(l) \\[2ex]
\dfrac{\partial \rho_s}{\partial t} = +v_s \dfrac{\partial \rho_s}{\partial l} + f_{cat}\rho_g - f_{res}\rho_s
\end{cases}
\tag{3.1}
$$

Note that polymerization and depolymerization changes the microtubule length l, but not the minus end position x_-.

Nucleation is represented by the term $+Q \cdot \delta(l)$ which appears as a term in the equation for growing microtubules. Q is specified by the particular scenario for microtubule nucleation that we wish to study. If we assume nucleation to be catalyzed by the local growing plus end density $C_g(t, x_+)$ (defined in Appendix C) and the cytoplasm to have a carrying capacity C_{cap} for growing plus end density, with $x_+ = x_- + l$ denoting the plus end position,

$$
Q(t, x_+) = v_g\, \rho_g(t,\ x_-,\ l = 0) = r \cdot C_g(t, x_+) \left(1 - \frac{C_g(t, x_+)}{C_{cap}} \right).
\tag{3.2}
$$
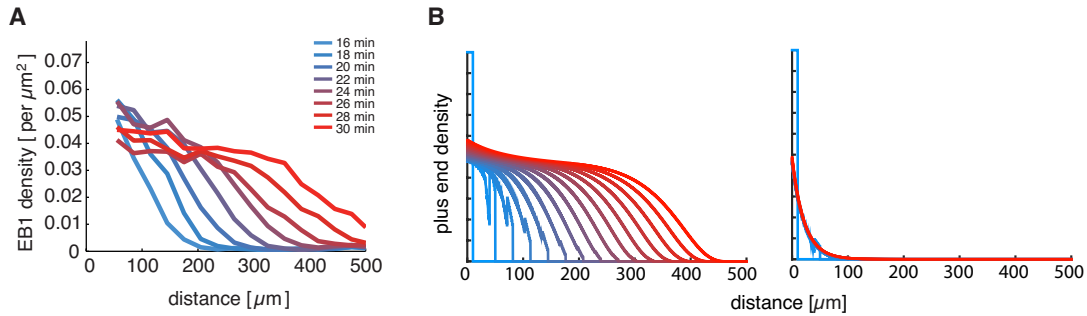
Figure 3.2: **The biophysical model recapitulates the key features of aster growth.** (A) Experimental measurements of EB1 comet density profiles during aster growth. Reprinted with permission from (Ishihara et al., 2014a). (B) Time evolution of growing plus end density profiles predicted by numerical simulations. Expansion of microtubule population was observed for parameters $v_g = 30, v_s = 40, f_{cat} = 3, f_{res} = 1, r = 2.5$ (left), but not when nucleate rate was lowered to $r = 1.0$ (right).

3.3   Aster Growth Dynamics

3.3.1   Rapid Aster Growth with Constant Microtubule Density

To study how our model predicts the distribution of microtubules over time, or aster growth, we numerically solved our continuum model with finite difference methods, varying the five parameters in our system. The initial condition was chosen to mimic a fixed number of "immortal" centrosomal microtubules with their minus ends at the origin. In some parameter sets, we observed the microtubule population to expand rapidly without dilution (Figure 3.2B left). This qualitatively recapitulated the rapid growth of large interphase asters observed in our reconstitution experiments (Figure 3.2A and Ishihara et al., 2014a). However, continuous aster growth was not always observed. When the nucleation rate was decreased, we observed the microtubule population to reach a steady-state profile confined near the origin (Figure 3.2B right). Thus, depending on the parameters, our model predicts two qualitatively different behaviors: (i) aster growth characterized by a linear increase radius without dilution of density and (ii) a steady-state aster with small, constant radius.

3.3.2 ASTER EXPANSION VELOCITY

As seen in our simulations (Figure 3.2B), aster growth is characterized by a traveling front that asymptotically approaches a constant shape and velocity in the long time limit. Thus, we use asymptotic analysis to find the exact solution of our continuum description (Appendix C). The aster expansion velocity V, defined as the rate at which the edge of microtubule population moves, is shown in equation C.21. This analytical expression predicts the overall aster growth rate as a function of microscopic parameters.

The effect of polymerization dynamics, represented by the mean polymerization rate J, on aster expansion velocity is shown in Figure 3.3A. In the absence of nucleation ($r = 0$), which is equivalent to the standard model of aster growth, we predict the aster radius to grow at rate $J > 0$, as expected. With nucleation ($r > 0$), we predict aster growth even for a finite range of $J < 0$. The maximum rate of aster expands is expected to be the polymerization rate of a single microtubule v_g. Our analytical solution correctly predicts this limit.

3.3.3 CRITICAL NUCLEATION RATE AND GAP VELOCITY

The aster expansion velocity V is an increasing function of the nucleation rate r (Figure 3.3B). This underscores the fact that nucleation positively contributes, not only to the density of microtubules at the periphery of a growing aster, but also to the rate at which the microtubule population spatially expand. For $J < 0$, we observe a qualitative transition in the aster growth. The aster expansion velocity is zero below a certain value of nucleation, while above this value, the velocity is positive. We define the minimal value of nucleation required for asters to continuously increase its radius as the critical nucleation rate r_c (Appendix C). It is given as

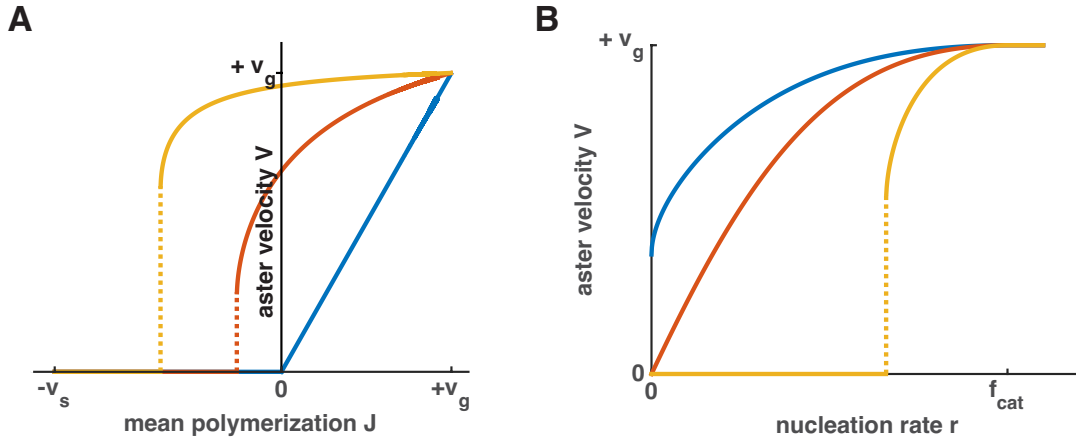$$r_c = f_{cat} - \frac{v_g}{v_s} f_{res}. \tag{3.3}$$

70

Figure 3.3: **Theoretical predictions of aster expansion velocity.** The rate of aster radius increase, or aster expansion velocity V, is shown as functions of mean polymerization rate J (A) and autocatalytic nucleation rate (B) according to our asymptotic analysis (see Appendix C). Parameters were fixed for $v_g = 30, v_s = 40, f_{cat} = 3.3$, varied for f_{res} and r. (A) Blue, orange, and yellow lines correspond to nucleation rates $r = 0, 1.2$, and 2.4. (B) Blue, orange, and yellow lines correspond to mean polymerization rates $J > 0, J = 0$, and $J < 0$

The significance of the critical nucleation rate is understood intuitively: increasing the parameters in favor of polymerization (v_g and f_{res}), lowers the threshold level of nucleation required for aster growth, while increasing the parameters in favor of depolymerization (v_s and f_{cat}), has the opposite effect. We also find that $r_c = 0$ when J = 0, suggesting that there is no critical nucleation rate for $J \geq 0$. This limit is consistent with the standard model with $J > 0$ and $r = 0$ where the aster radius increases albeit with radial dilution of microtubule density (Figure 3.1B). The critical nucleation rate conveys the main implication of our theory: the precise balance between polymerization dynamics and autocatalytic nucleation defines the quantitative condition for continuous aster growth.

At the critical nucleation rate, the aster expansion velocity V takes a positive, non-zero value. We term this the "gap velocity":

$$V_{gap} \equiv \lim_{r \to r_c} V = \frac{-v_g v_s (v_g f_{res} - v_s f_{cat})}{v_g^2 f_{res} + v_s^2 f_{cat}}. \tag{3.4}$$

71

For an aster to grow under our assumptions, it needs to expand above this minimum velocity regardless of the exact value of the nucleation rate as long as $r > r_c$.

3.3.4 Inferring the Rate of Nucleation

Our biophysical model offers an attractive explanation aster growth by assuming autocatalytic nucleation. How plausible is our model in light of experimental measurements? The expression for the aster expansion velocity (equation (C.21)) and gap velocity (3.4) maybe used to infer the rate of nucleation. Table 1 summarizes the parameter values that we determined previously (Ishihara et al., 2014a) and in this study. We assume a range of values for the rescue rate f_{res} in the following way: the lower bound was found by asserting that the observed expansion velocity is greater than the gap velocity; the upper bound was determined by setting $J = 0$, assuming bounded regime of dynamic instability (Ishihara et al., 2014a). In this way, we infer the value of autocatalytic nucleation at 2.7-3.1 min^{-1}. Our inferred value of autocatalytic nucleation is comparable to previous reports: 1.5 min^{-1} (Clausen and Ribbeck, 2007) and $\sim$1 min^{-1}(Petry et al., 2013) in meiotic egg extract supplemented with RanGTP. $\sim$0.5 min^{-1} for the spontaneous nucleation in interphase egg extract (Ishihara et al., 2014a). Thus, our model explains aster growth with realistic parameter values.

Quantity	Symbol	Value	Comment
Aster expansion velocity	V	22 μm/min	Direct measurement (Ishihara et al., 2014a)
Polymerization rate	v_g	30 μm/min	Direct measurement (Ishihara et al., 2014a)
Depolymerization rate	v_s	42 μm/min	Direct measurement (Ishihara et al., 2014a)
Catastrophe rate (growing→shrinking)	f_{cat}	3.3 min^{-1}	From EB1 comet lifetimes (see Methods)
Rescue rate (shrinking→growing)	f_{res}	0.81 - 4.6 min^{-1}	$V_{gap} < V$ and bounded dynamics ($J < 0$)
Autocatalytic nucleation rate	r	2.7 - 3.1 min^{-1}	Inferred with equation (C.21)

Table 3.1: **Model parameters used to describe aster growth reconstituted in frog egg extract.**

3.4 Discussion

In this study, we constructed a biophysical framework to describe the growth of microtubule asters that span the enormous cytoplasms of embryonic cells. As the standard model of aster growth was clearly insufficient to explain the high microtubule density and the rapid increase in aster radius, we asked if these issues could be resolved by hypothesizing autocatalytic microtubule nucleation and thus viewing aster growth as a collective behavior of microtubules (Figure 3.1). Through simulations (Figure 3.2) and analytical approaches (Figure 3.3), we found the model to qualitatively recapitulate the large aster growth in a parameter-dependent manner. Importantly, the "no growth-to-growth" transition of aster dynamics rested on whether the nucleation rate was above a threshold value defined by the polymerization dynamics, the critical nucleation rate (3.3). Our model exhibits these behaviors with experimentally determined parameters (Table 3.1). Our biophysical framework has connections to reaction-transport models in physics (van Saarloos, 2003) and engineering (Méndez et al., 2010), demonstrating the usefulness of such approaches to understand self-organization in cell biology.

How do large cells control aster size during rapid divisions? We summarize our theoretical implications with a phase diagram for aster growth (Figure 3.4). Small mitotic asters are most consistent with the regime of bounded polymerization dynamics $J < 0$ and low nucleation rate (bounded aster). The cell cycle change from mitosis to interphase alters the polymerization dynamics in favor of polymerization (Belmont et al., 1990; Verde et al., 1992), increasing the mean polymerization rate J. Whether J increases to a positive value is unclear. Though one study suggested the interphase to be in the unbounded regime of dynamic instability (Verde et al., 1992), our measurements *in situ* using modern methods (Table 3.1) differ greatly from theirs. Further, a scenario of $J > 0$ is inconsistent with the apparent steady-state for microtubule polymer and plus end density at the interior of large asters (Ishihara et al., 2014a). Through theoretical analysis, we discovered a new sce-

nario, in which continuous aster growth is supported by autocatalytic nucleation $r > r_c$ even when $J < 0$. Here, the polymerization dynamics predict individual microtubule to be bounded in length, but the overall aster grows in an unbounded manner. We call this the "collective growth" regime of aster growth, and propose it as the mechanism underlying the growth of large interphase asters. It is unclear how the cell cycle alters the nucleation rate, but our inferred rate in interphase is comparable in magnitude to other reports in mitosis. Our theory points to the possibility that, even if the nucleation rate is unchanged, cells regulate aster size by lowering the threshold value of nucleation required for aster growth.

Assembly of a large structure by a population of short, interacting filaments is reminiscent of how mitotic spindles self-assemble. Perhaps, this may be the only reliable way to assemble cytoskeletal structures that exceeds the length scales of individual filament dynamics. Due to such dynamic architecture, the spindle is known to have unique physical properties such as self-repair, fusion (Gatlin et al., 2009) and scaling (Wühr et al., 2008; Hazel et al., 2013; Good et al., 2013). Our proposed mechanism of aster growth has no theoretical limit on its final size, but the repeating pattern of short microtubules potentially explains its rapid disassembly. Finally, a physically interconnected meshwork of microtubules prompts us to rethink how mechanical forces may be transduced across the entire cell.

3.5   Materials and Methods

Experimental Data

Interphase microtubule asters were reconstituted in *Xenopus* egg extract as described previously with use of p150-CC1 to inhibit dynein mediated microtubule sliding (Field et al., 2014; Ishihara et al., 2014a). Catastrophe rates were estimated from time lapse images of EB1 comets that localize to growing plus ends(Tirnauer et al., 2004). Spinning disc confocal microscopy was performed on a
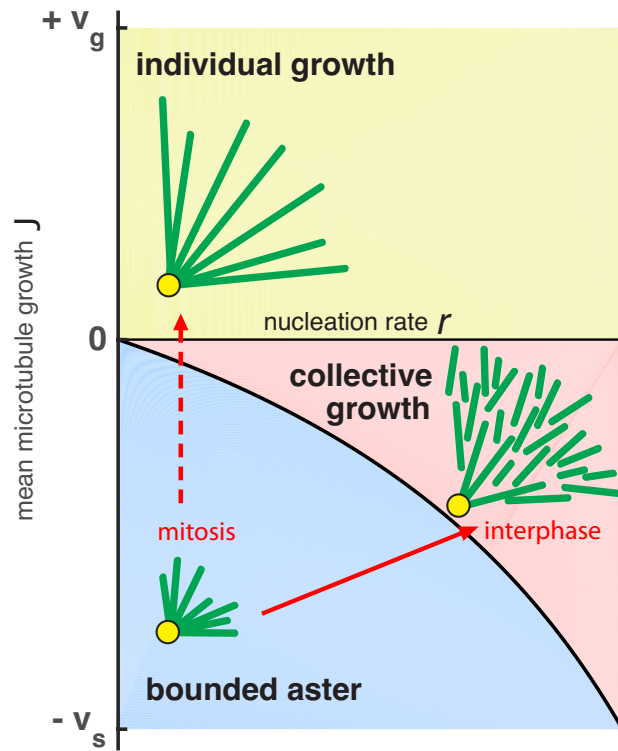
Figure 3.4: **Phase diagram for aster growth.** Aster growth is predicted by the balance of polymerization dynamics and autocatalytic nucleation. With mean polymerization dynamics $J < 0$ and low nucleation r, small asters with steady-state radius is predicted (bounded aster). With $J > 0$, the aster grows in radius according, but without nucleation microtubule density will decrease in the aster periphery (yellow region, individual growth). With sufficiently strong nucleation r above the critical nucleation rate r_c equation (3.3), a bounded aster transitions into a continuously expanding aster composed of relatively short microtubules (blue region, collective growth).

Nikon Ti motorized inverted microscope equipped with Perfect Focus, a Prior Proscan II motorized stage, Yokagawa CSU-X1 spinning disk confocal with Spectral Applied Research Aurora Borealis modification, Spectral Applied Research LMM-5 laser merge module with AOTF controlled solid state lasers: 488nm (100mW), 561nm (100mW), and Hamamatsu ORCA-AG cooled CCD camera. EB1-GFP and EB1-mApple were purified as in (Petry et al., 2011), used at a final concentration of 100 nM, and imaged every 2 sec with a 60x Plan Apo 1.40 N.A objective with 2x2 binning. EB1 tracks were analyzed with PlusTipTracker (Applegate et al., 2011). Lifetime distributions of the EB1 tracks were fitted to an exponential function to estimate the catastrophe rate.

NUMERICAL SIMULATION

We implemented a finite difference method with fixed time steps to numerically solve the continuum model described in Appendix C. Plus end positions were updated by shifting the elements in matrices rather than using standard stencil update rules. Catastrophe, rescue events changed the number of growing and shrinking microtubules. The algorithm was implemented using MATLAB (Mathworks).

ACKNOWLEDGMENTS

REFERENCES

Akhmanova, A., and M.O. Steinmetz. 2015. Control of microtubule organization and dynamics: two ends in the limelight. Nat Rev Mol Cell Biol.

Applegate, K.T., S. Besson, A. Matov, M.H. Bagonis, K. Jaqaman, and G. Danuser. 2011. plusTip-Tracker: Quantitative image analysis software for the measurement of microtubule dynamics. J. Struct. Biol. 176:168-184.

Belmont, L.D., A.A. Hyman, K.E. Sawin, and T.J. Mitchison. 1990. Real-time visualization of cell cycle-dependent changes in microtubule dynamics in cytoplasmic extracts. Cell. 62:579-589.

Bicout, D. 1997. Green's functions and first passage time distributions for dynamic instability of microtubules. Physical Review E.

Brinkley, B.R. 1985. Microtubule organizing centers. Annu. Rev. Cell Biol. 1:145-172.

Brugues, J., and D. Needleman. 2014. Physical basis of spindle self-organization. Proceedings of the National Academy of Sciences of the United States of America.

Brugues, J., V. Nuzzo, E. Mazur, and D.J. Needleman. 2012. Nucleation and Transport Organize Microtubules in Metaphase Spindles. Cell. 149:554-564.

Clausen, T., and K. Ribbeck. 2007. Self-organization of anastral spindles by synergy of dynamic instability, autocatalytic microtubule production, and a spatial signaling gradient. PLoS ONE. 2:e244.

Dogterom, M., and S. Leibler. 1993. Physical aspects of the growth and regulation of microtubule structures. Phys Rev Lett. 70:1347-1350.

Efimov, A., A. Kharitonov, N. Efimova, J. Loncarek, P.M. Miller, N. Andreyeva, P. Gleeson, N. Galjart, A.R.R. Maia, I.X. McLeod, J.R. Yates, H. Maiato, A. Khodjakov, A. Akhmanova, and I. Kaverina. 2007. Asymmetric CLASP-dependent nucleation of noncentrosomal microtubules at the trans-Golgi network. Dev Cell. 12:917-930.

Etienne-Manneville, S. 2013. Microtubules in Cell Migration. Annu. Rev. Cell Dev. Biol. 29:471-499.

Field, C.M., P.A. Nguyen, K. Ishihara, A.C. Groen, and T.J. Mitchison. 2014. *Xenopus* egg cytoplasm with intact actin. Meth. Enzymol. 540:399-415.

Gatlin, J.C., A. Matov, A.C. Groen, D.J. Needleman, T.J. Maresca, G. Danuser, T.J. Mitchison, and E.D. Salmon. 2009. Spindle fusion requires dynein-mediated sliding of oppositely oriented microtubules. Curr Biol. 19:287-296.

Good, M.C., M.D. Vahey, A. Skandarajah, D.A. Fletcher, and R. Heald. 2013. Cytoplasmic volume modulates spindle size during embryogenesis. Science. 342:856-860.

Grigoriev, I., S.M. Gouveia, B. Van der Vaart, and J. Demmers. 2008. STIM1 Is a MT-Plus-End-Tracking Protein Involved in Remodeling of the ER. Current Biology.

Grill, S.W., and A.A. Hyman. 2005. Spindle positioning by cortical pulling forces. Dev Cell. 8:461-465.

Hazel, J., K. Krutkramelis, P. Mooney, M. Tomschik, K. Gerow, J. Oakey, and J.C. Gatlin. 2013. Changes in cytoplasmic volume are sufficient to drive spindle scaling. Science. 342:853-856.

Ishihara, K., P.A. Nguyen, A.C. Groen, C.M. Field, and T.J. Mitchison. 2014a. Microtubule nucleation remote from centrosomes may explain how asters span large cells. Proceedings of the National Academy of Sciences of the United States of America. 111:17715-17722.

Ishihara, K., P.A. Nguyen, M. Wühr, A.C. Groen, C.M. Field, and T.J. Mitchison. 2014b. Organization of early frog embryos by chemical waves emanating from centrosomes. Philosophical Transactions of the Royal Society B: Biological Sciences. 369.

Keating, T.J., and G.G. Borisy. 1999. Centrosomal and non-centrosomal microtubules. Biol. Cell. 91:321-329.

Keating, T.J., J.G. Peloquin, V.I. Rodionov, D. Momcilovic, and G.G. Borisy. 1997. Microtubule release from the centrosome. Proceedings of the National Academy of Sciences of the United States of America. 94:5078-5083.

Loose, M., K. Kruse, and P. schwille. 2011. Protein Self-Organization: Lessons from the Min System. Biophysics.

Loughlin, R., R. Heald, and F. Nédélec. 2010. A computational model predicts *Xenopus* meiotic spindle organization. The Journal of cell biology. 191:1239-1249.

Méndez, V., S. Fedotov, and W. Horsthemke. 2010. Reaction-Transport Systems. Springer. 1 pp.

Mitchison, T., M. Wühr, P. Nguyen, K. Ishihara, A. Groen, and C.M. Field. 2012. Growth, interaction, and positioning of microtubule asters in extremely large vertebrate embryo cells. Cytoskeleton.

69:738-750.

Neumüller, R.A., and J.A. Knoblich. 2009. Dividing cellular asymmetry: asymmetric cell division and its implications for stem cells and cancer. Genes Dev. 23:2675-2699.

Nguyen, P.A., A.C. Groen, M. Loose, K. Ishihara, M. Wühr, C.M. Field, and T.J. Mitchison. 2014. Spatial organization of cytokinesis signaling reconstituted in a cell-free system. Science. 346:244-247.

Petry, S., A.C. Groen, K. Ishihara, T.J. Mitchison, and R.D. Vale. 2013. Branching microtubule nucleation in *Xenopus* egg extracts mediated by augmin and TPX2. Cell. 152:768-777.

Petry, S., C. Pugieux, F.J. Nédélec, and R.D. Vale. 2011. Augmin promotes meiotic spindle formation and bipolarity in *Xenopus* egg extracts. Proceedings of the National Academy of Sciences of the United States of America. 108:14473-14478.

Roll-Mecak, A., and F.J. McNally. 2010. Microtubule-severing enzymes. Curr Opin Cell Biol. 22:96-103.

Tirnauer, J.S., E.D. Salmon, and T.J. Mitchison. 2004. Microtubule plus-end dynamics in *Xenopus* egg extract spindles. Mol Biol Cell. 15:1776-1784.

van Saarloos, W. 2003. Front propagation into unstable states. Physics Reports. 386:29-222.

Verde, F., M. Dogterom, E. Stelzer, E. Karsenti, and S. Leibler. 1992. Control of microtubule dynamics and length by cyclin A- and cyclin B-dependent kinases in *Xenopus* egg extracts. The Journal of cell biology. 118:1097-1108.

Wang, S., F.B. Romano, C.M. Field, T.J. Mitchison, and T.A. Rapoport. 2013. Multiple mechanisms determine ER network morphology during the cell cycle in *Xenopus* egg extracts. The Journal of cell biology. 203:801-814.

Waterman-Storer, C., D.Y. Duey, K.L. Weber, J. Keech, R.E. Cheney, E.D. Salmon, and W.M. Bement. 2000. Microtubules remodel actomyosin networks in *Xenopus* egg extracts via two mechanisms of F-actin transport. The Journal of cell biology. 150:361-376.

Waterman-Storer, C.M., and E.D. Salmon. 1998. Endoplasmic reticulum membrane tubules are distributed by microtubules in living cells using three distinct mechanisms. Curr Biol. 8:798-806.

Weiner, O.D., W.A. Marganski, L.F. Wu, S.J. Altschuler, and M.W. Kirschner. 2007. An Actin-Based Wave Generator Organizes Cell Motility. PLoS Biol. 5:e221.

Wilson, E.B. 1896. The Cell in development and inheritance. Macmillan, New York. 1 pp.

Wühr, M., E.S. Tan, S.K. Parker, H.W. Detrich, and T.J. Mitchison. 2010. A model for cleavage plane determination in early amphibian and fish embryos. Curr Biol. 20:2040-2045..

Wühr, M., S. Dumont, A.C. Groen, D.J. Needleman, and T.J. Mitchison. 2009. How does a millimeter-sized cell find its center? Cell Cycle. 8:1115-1121.

Wühr, M., Y. Chen, S. Dumont, A.C. Groen, D.J. Needleman, A. Salic, and T.J. Mitchison. 2008. Evidence for an upper limit to mitotic spindle length. Curr Biol. 18:1256-1261.

A

Additional publications from my graduate work

Research Articles

Petry, S., A.C. Groen, K. Ishihara, T.J. Mitchison, and R.D. Vale. 2013. Branching microtubule nucleation in *Xenopus* egg extracts mediated by augmin and TPX2. Cell. 152:768-777

Nguyen, P.A., A.C. Groen, M. Loose, K. Ishihara, M. Wühr, C.M. Field, and T.J. Mitchison. 2014. Spatial organization of cytokinesis signaling reconstituted in a cell-free system. Science. 346:244-247

Wühr, M., T. Güttler, L. Peshkin, G.C. McAlister, M. Sonnett, K. Ishihara, A.C. Groen, M. Presler, B.K. Erickson, T.J. Mitchison, M.W. Kirschner, and S.P. Gygi. 2015. The Nuclear Proteome of a Vertebrate. Curr Biol. 25:2663-2671

Reviews

Mitchison, T., M. Wühr, P. Nguyen, K. Ishihara, A. Groen, and C.M. Field. 2012. Growth, interaction, and positioning of microtubule asters in extremely large vertebrate embryo cells. Cytoskeleton. 69:738-750

Mitchison, T.J., K. Ishihara, P. Nguyen, and M. Wühr. 2015. Size Scaling of Microtubule Assemblies in Early *Xenopus* Embryos. Cold Spring Harbor perspectives in biology

Book Chapters

Field, C.M., P.A. Nguyen, K. Ishihara, A.C. Groen, and T.J. Mitchison. 2014. *Xenopus* egg cytoplasm with intact actin. Meth. Enzymol. 540:399-415

Groen, A.C., P.A. Ngyuen, C.M. Field, K. Ishihara, and T.J. Mitchison. 2014. Glycogen-supplemented mitotic cytosol for analyzing *Xenopus* egg microtubule organization. Meth. Enzymol. 540:417-433

B

Supplemental Materials for Chapter 2
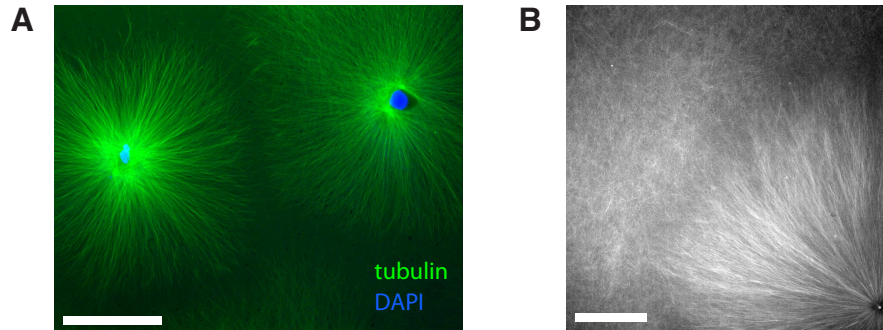
Figure B.1: **Asters organized by demembranated frog sperm.** (A) Asters organized by demembranated frog sperm contain a pair of centrioles. Note that each sperm chromatin (blue) is associated with two independent nucleating centers that radiate microtubules (green). (B) At later time points, populations of microtubules often appear in the background before the aster reaches that location and interrupt aster growth. Scale bar 100 μm.
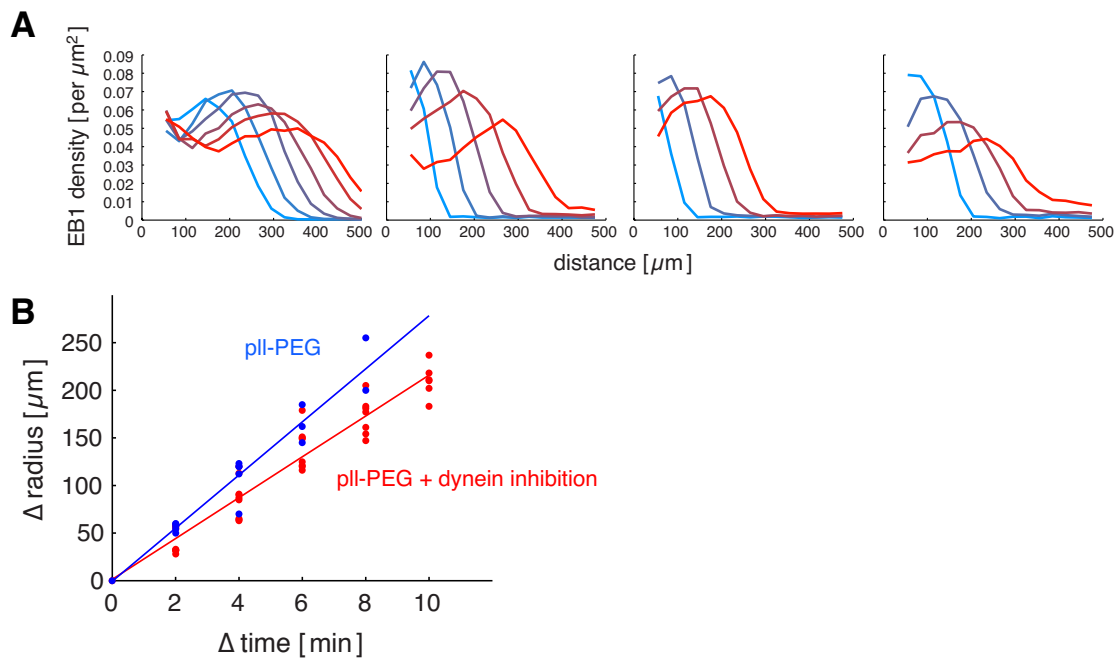
Figure B.2: **EB1 density plots of aster growth with dynein-mediated microtubule sliding.** (A) EB1 density plots of aster growth where dynein-mediated microtubule sliding was allowed. Cover slips were treated with PLL-PEG. Curves in each plot are 2 min apart. (B) Comparison of half-max positions over time during aster growth with and without dynein activity. Blue dots represent data from n = 5 aster reaction on PLL-PEG coverslips. Red dots represent data from n = 9 aster reactions on PLL-PEG coverslips, treated with p150-CC1 to inhibit dynein activity.

Figure B.3: More examples of total EB1 comets vs predicted contribution of the Aurora kinase A bead during aster growth. (A) More examples of total EB1 comets (blue) vs predicted contribution of the Aurora kinase A bead (red) during aster growth as in Figure 2.5B. These plots correspond to the first three asters whose EB1 density plots are shown in Figure 2.4D. (B) Bead:total ratio as in Figure 2.5B inset for multiple asters.

B.2 SUPPLEMENTAL MOVIES

B.2.1 MOVIE B.1

Fluorescent speckle microscopy movie of an aster assembled under untreated coverslips (same aster as Figure 2.2B). Images were collected every 4 sec. Resolution is 0.2 μm/pixel.

B.2.2 MOVIE B.2

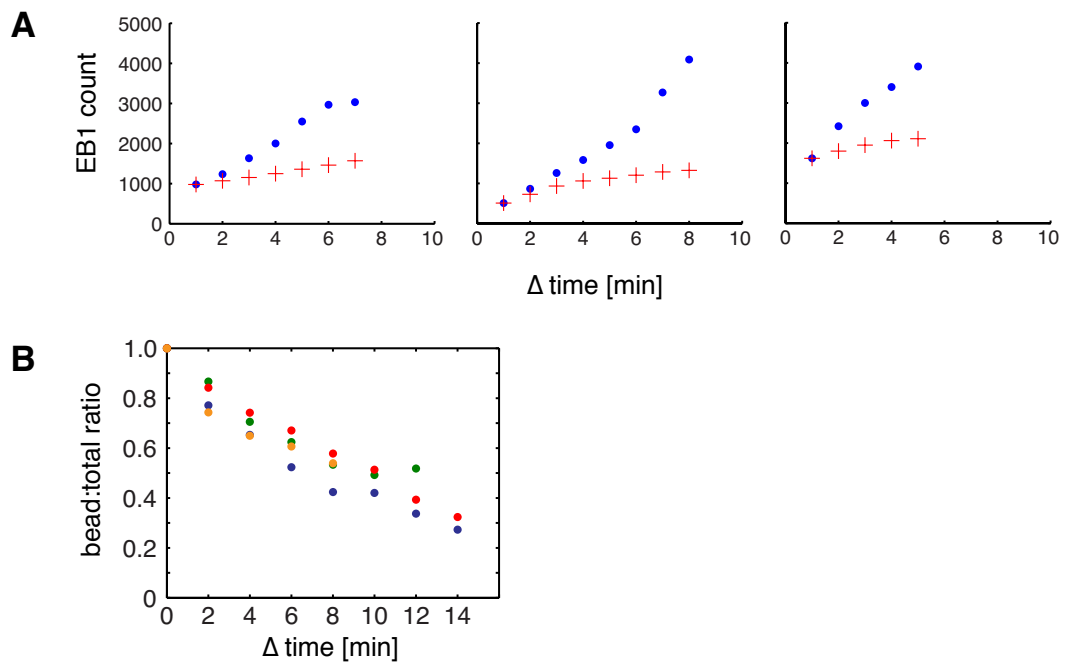Fluorescent speckle microscopy movie of an aster treated with p150-CC1 to inhibit dynein motor activity (same aster as Figure 2.2D). Images were collected every 4 sec. Resolution is 0.2 μm/pixel.

B.2.3 MOVIE B.3

Fluorescent speckle microscopy movie of an aster assembled between coverslips passivated with poly-L-lysine PEG (same aster as Figure 2.2F). Images were collected every 4 sec. Resolution is 0.2 μm/pixel.

B.2.4 MOVIE B.4

TIRF microscopy movie of Alexa647-labeled tubulin showing dynamic microtubules in aster (same aster as Figure 2.3). Images were collected continuously every 500 ms. Resolution is 107 nm/pixel.

B.2.5 MOVIE B.5

Spatial map of polymerization. Movie showing the pixels with positive values of intensity differences of subsequent frames in Movie S4. Difference images were constructed as described in methods.

B.2.6 MOVIE B.6

Spatial map of depolymerization. Movie showing the pixels with negative values of intensity differences of subsequent frames in Movie S4. Difference images were constructed as described in methods.

Supplemental movies are also available at

www.pnas.org/lookup/suppl/doi:10. 1073/pnas.1418796111/-/DCSupplemental

C

Continuum description of aster growth

C.1 Coupling microtubule polymerization dynamics and autocatalytic nucleation

To describe our system of microtubules, we define the mean-field variable $\rho_g(t, x_-, l)$ which represents the local density of growing plus ends of length l with its corresponding minus end at position r_- at time t. Similarly, we define the shrinking plus end variable $\rho_s(t, x_-, l)$. We assume that all microtubules have the same polarity, namely that all microtubules have their plus ends pointing outwards. Given this polarity, the plus end position of a microtubule is $x_+ = x_- + l$. The evolution of our system is described as follows:

$$\begin{cases} \dfrac{\partial \rho_g}{\partial t} = -v_g \dfrac{\partial \rho_g}{\partial l} - f_{cat}\rho_g + f_{res}\rho_s \\[2mm] \dfrac{\partial \rho_s}{\partial t} = +v_s \dfrac{\partial \rho_s}{\partial l} + f_{cat}\rho_g - f_{res}\rho_s \end{cases} \tag{C.1}$$

Note that the above expression represents an infinite set of equations valid for the continuum $x_- \geq 0$.

We also impose the boundary condition $\rho_g(t,\, x_-,\, l=0) = \frac{Q}{v_g}$, where Q is the nucleation rate in units [ends/time]. Note that the flux of new microtubules into the system is $v_g\, \rho_g(t,\, x_-,\, l = 0)$.[*] We assume that when a plus end shrinks back to its minus end, the microtubule disappears (absorbing boundary condition).

Microtubule nucleation is defined as the birth of length zero growing microtubules and, in general, may depend on ρ_g, ρ_s. In the following sections, we assume nucleation process as bifurcation of growing plus ends. Nucleation is expressed as a logistic function of local growing plus end density regardless of their corresponding microtubule length with carrying capacity of the system as C_{cap}.

$$Q(t, x_+) = v_g\, \rho_g(t,\, x_-,\, l = 0) = r \cdot C_g(t, x_+) \left(1 - \frac{C_g(t, x_+)}{C_{cap}} \right) \tag{C.2}$$

$C_g(t, x_+)$ denotes the local growing plus end density at position x_+ and time t. By equating the plus end density times the surface area of a sphere of radius x_+ to the integration of $\rho_g(t, x_-, l)$ whose plus ends happens be positioned at distance x_+ , we obtain the following expression for local growing plus end density:

$$C_g(t, x_+) = \int_0^{+\infty} \int_0^{x_+} \rho_g(t, x_-, l) \cdot \delta(x_+ - x_- - l)\, dx_-\, dl \tag{C.3}$$

Similarly, we define the shrinking plus end density $C_s(t, x_+)$.

---

[*]An alternative way to consider nucleation is in the form of an additional term in the right hand side of the first equation of (C.1) such as $Q \cdot \delta(l)$ with the Dirac delta function. This yields the equivalent equation when it is transformed later.

Thus far, we have assumed a one-dimensional system with x_+ and x_- being scalar. This simplifies the analysis in the following sections, but we note that the main results still hold for higher dimensions in cylindrical or spherical coordinates in the limit of large radial distance $|x|$ (treating x as a vector that specifies position). For these higher dimensions d=2,3..., we rewrite (C.3) as

$$C_g(t, |x_+|) = \frac{1}{|x_+|^{d-1}} \int_0^{+\infty} \int_0^{|x_+|} \rho_g(t, |x_-|, l) \cdot \delta(|x_+| - |x_-| - l) \, |x_+|^{d-1} \, d|x_-| \, dl.$$

C.2 BOUNDED AND UNBOUNDED REGIMES OF POLYMERIZATION DYNAMICS

In the absence of nucleation ($r = 0$), the dynamics of our system is goverened solely by microtubule plus end dynamics. Imagine a scenario where there is a fixed number of microtubules in the system, and that all their minus ends are at the origin. Further, let's assumed that when plus ends shrink back to their minus ends, they instantly transition to a growing state, akin to a reflective boundary condition at the origin. In such cases, two qualitatively different regimes of plus end dynamics have been highlighted by others (Dogterom and Leibler, 1993; Verde et al., 1992; Bicout, 1997). Consider the time weighted average of polymerization and depolymerization, which we call the mean polymerization rate J.

$$\text{mean polymerization rate:} \quad J = \frac{v_g f_{res} - v_s f_{cat}}{f_{res} + f_{cat}}$$

J is essentially the directional bias of the plus end dynamics, the drift term of the biased random walk. When $J < 0$, every microtubule will eventually shrink back to the origin. This is the so-called bounded regime of dynamic instability, in which the length of individual microtubules are found to be exponentially distributed with an average length of $\langle l \rangle = \frac{-v_g v_s}{v_g f_{res} - v_s f_{cat}}$. When $J > 0$, eventually all microtubules will be long enough to be far from the origin. Thus, there is no steady-

state length distribution and the average length increases at rate J, and this is called the unbounded regime of dynamic instability.

C.3 Aster growth dynamics with autocatalytic microtubule nucleation

Here, we analyze the behavior of the system when polymerization dynamics and autocatalytic microtubule nucleation are allowed. Our intuition is that microtubule nucleation will produce microtubules at distances far from the origin, and that with high enough nucleation, the population of microtubules will start to move away from the origin as a self-propagating wave. For the microtubule nucleation of form (C.2), we first show that the full analytical solution for the spatiotemporal evolution may be solved. Next, to detemine the long time behavior of the wave front, namely the aster expansion velocity, we perform asympotic analysis. This leads us to the concept of the critical nucleation rate, which aptly summarizes the condition that determines aster growth (linear increase in radius), or no growth (constant radius).

C.3.1 Solution of the system

We apply the Laplace transform to (C.1) in the following way: time domain $t \rightarrow s$, spatial domain $x_- \rightarrow k$ and length domain $l \rightarrow q$. Our system recast in $\rho_g(s, k, q)$ and $\rho_s(s, k, q)$ becomes

$$
\begin{cases}
s\rho_g - \rho_g(t = 0, k, q) = -v_g q \rho_g + v_g \rho_g(s, k, l = 0) - f_{cat}\rho_g + f_{res}\rho_s \\
s\rho_s - \rho_s(t = 0, k, q) = +v_s q \rho_s - v_s \rho_s(s, k, l = 0) + f_{cat}\rho_g - f_{res}\rho_s
\end{cases}
\tag{C.4}
$$

We can not directly solve the system (C.4) for $\rho_g(s, k, q)$ and $\rho_s(s, k, q)$ as $\rho_g(s, k, l = 0)$ and $\rho_s(s, k, l = 0)$ are unknown. However, we demonstrate that the system can be closed for the local plus end densities $C_g(s, k)$ and $C_s(s, k)$ given our particular form of nucleation rate (C.2). We substitute this solution back to C.4 and obtain the full solution of the system in terms of ρ_g and ρ_s.

First, let us consider the transformation of $C_g(t, x_+)$ in the spatial domain $x_+ \to k$.

$$
\begin{aligned}
C_g(t, k) &= \int_0^{+\infty} e^{-kx_+} dx_+ \, C_g(t, x_+) \\
&= \int_0^{+\infty} e^{-kx_+} dx_+ \int_0^{+\infty} \int_0^{+\infty} \delta(x_+ - x_- - l) \, dl \, dr_- \, \rho_g(t, x_-, l) \\
&= \int_0^{+\infty} \int_0^{+\infty} da \, dl \, \rho_g(t, x_-, l) \, e^{-kx_-} e^{-kl} \\
&= \int_0^{+\infty} dl \, \rho_g(t, k, l) \, e^{-kl} \\
&= \rho_g(t, k, k)
\end{aligned}
$$

We apply the same transform to $C_s(t, x_+)$ and obtain the following:

$$
C_g(s, k) = \rho_g(s, k, k) \quad \text{and} \quad C_s(s, k) = \rho_s(s, k, k) \tag{C.5}
$$

Thus, we find that the local plus end density $C_g(s, k)$ is equivalent to a special subset of $\rho_g(s, k, q)$ that is $\rho_g(s, k, k)$ where the spatial and length domains are coupled to each other. Applying (C.5) and $k = q$ to (C.4), we obtain

$$
\begin{cases}
sC_g - C_g(t = 0, k) = -v_g k C_g + v_g C_g(s, k, l = 0) - f_{cat} C_g + f_{res} C_s \\
sC_s - C_s(t = 0, k) = +v_s k C_s - v_s C_s(s, k, l = 0) + f_{cat} C_g - f_{res} C_s
\end{cases}
$$

Note that the term corresponding to growing plus ends at $l = 0$ is equivalent to our defintion of nucleation rate (C.2). Here, we substitute the linearized form $v_g \, \rho_g(s, \, k, \, l = 0) = r \cdot C_g(s, k)$ which is valid for small $C_g(s, x)$ or at the leading edge of the aster. The term corresponding to shrinking plus ends at $l = 0$ is not specified in our system. Later, we derive the condition for $C_s(s, k, l = 0)$ that guarantees physical plausibility. Assuming that the initial conditions $\rho_g^0 =$

$\rho_g(t=0,k)$ and $\rho_s^0 = \rho_s(t=0,k)$ are known, we arrive at the subproblem:

$$
A_r \begin{pmatrix} C_g(s,k) \\ C_s(s,k) \end{pmatrix} = \begin{pmatrix} \rho_g^0 \\ \rho_s^0 - v_s\rho_s(l=0) \end{pmatrix},
$$

$$
\text{where } A_r = \begin{bmatrix} s + v_g k + f_{cat} - r & -f_{res} \\ -f_{cat} & s - v_s k + f_{res} \end{bmatrix}. \tag{C.6}
$$

This system is solved by matrix inversion. The solution for growing plus end density is

$$
C_g(s,k) = \frac{1}{\det(A_r)} \left[A_{r,22} \cdot \rho_g^0 - A_{r,12}(\rho_s^0 - v_s\rho_s(l=0)) \right]. \tag{C.7}
$$

With the knowledge of $C_g(s,k) = \rho_g(s,k,k)$, we proceed to find the general solution $\rho_g(s,k,q)$ by returning to the full problem (C.1). Arranging the known quantitites to the right hand side, the rewritten problem is

$$
A \begin{pmatrix} \rho_g(s,k,q) \\ \rho_s(s,k,q) \end{pmatrix} = \begin{pmatrix} \rho_g^0 + rC_g(s,k) \\ \rho_s^0 - v_s\rho_s(l=0) \end{pmatrix},
$$

$$
\text{where } A = \begin{bmatrix} s + v_g q + f_{cat} & -f_{res} \\ -f_{cat} & s - v_s q + f_{res} \end{bmatrix}. \tag{C.8}
$$

For the solution of plus end density, we substitute our solution of $C_g(s,k)$ and obtain

$$\rho_g(s,k,q) = \frac{1}{\det(A)} \left[A_{22}(\rho_g^0 + rC_g(s,k)) - A_{12}(\rho_s^0 - v_s\rho_s(l=0)) \right]$$

$$= \frac{1}{\det(A)} \left(A_{22}\rho_g^0 - A_{12}\rho_s^0 \right) + \frac{A_{12}}{\det(A)} v_s\rho_s(l=0) +$$

$$\frac{1}{\det(A)} \frac{rA_{22}}{\det(A_r)} \left(A_{r,22}\rho_g(t=0,k,k) - A_{r,12}\rho_s(t=0,k,k) + A_{r,12}v_s\rho_s(l=0) \right)$$

$$= \frac{1}{\det(A)} \left(A_{22}\rho_g^0 - A_{12}\rho_s^0 \right) + v_s\rho_s(l=0) \left(\frac{A_{12}}{\det(A)} + \frac{rA_{22}A_{r,12}}{\det(A)\det(A_r)} \right)$$

$$+ \frac{rA_{22}}{\det(A)\det(A_r)} \left(A_{r,22}\rho_g(t=0,k,k) - A_{r,12}\rho_s(t=0,k,k) \right).$$

$$\tag{C.9}$$

C.3.2 Physical plausibility at $l \to \infty$

In (C.9), we still have one unknown $\rho_s(l=0)$, which we determine by imposing a physical plausibility condition. Namely, we impose that the number of infinitely long microtubules are zero by requesting that the solution ρ_g (and ρ_s) decays as $l \to \infty$. To see this, we apply the inverse Laplace transform $q \to l$,

$$\rho_g(s,k,l) = \frac{1}{2\pi i} \int_{\gamma-i\infty}^{\gamma+i\infty} e^{ql} dq\, \rho_g(s,k,q)$$

$$= \sum_{q_j} \underset{q_j}{\mathrm{Res}}\, e^{ql}\rho_g(s,k,q)$$

$$\tag{C.10}$$

Note that the only term that depends on q in (C.9) is $\det(A)$. $\det(A) = 0 \Leftrightarrow$

$$q^2 v_g v_s - q[s(v_g - v_s) + v_g f_{res} - v_s f_{cat}] - [s^2 + s(f_{cat} + f_{res})] = 0 \tag{C.11}$$

This equation has two roots $q_+ > 0$ and $q_- < 0$, since

$$q_+ q_- = -\frac{s^2 + s(f_{cat} + f_{res})}{v_g v_s} < 0.$$

Therefore, the $\rho_g(s, k, l)$ takes the form $\rho_g(s, k, l) = e^{q_+ l}\rho_g(s, k, q_+) + e^{q_- l}\rho_g(s, k, q_-)$.

We require that $\rho_g(s, k, l)$ takes a finite value in the limit of $l \to \infty$ by setting the the coefficient for $e^{q_+ l}$ to zero, in other words $\rho_g(s, k, q_+) = 0$. Thus with A^+ denoting matrix A when $q = q_+$ and $\rho_g^{0,+} = \rho_g(t = 0, k, q^+)$, we request the following condition:

$$
\begin{aligned}
&A_{22}^+ \rho_g^{0,+} - A_{12}^+ \rho_s^{0,+} + v_s\rho_s(l = 0)(A_{12}^+ + \frac{rA_{22}^+ A_{r,12}}{\det(A_r)}) \\
&+ \frac{rA_{22}^+}{\det(A_r)}(A_{r,22}\rho_g(t = 0, k, k) - A_{r,12}\rho_s(t = 0, k, k)) = 0
\end{aligned}
\tag{C.12}
$$

Recall that $\rho_s(l = 0)$ was introduced as an unknown in our system via Laplace transform despite the absence of a *bona fide* boundary condition for shrinking microtubules of length zero. We may now solve the above equation for $\rho_s(l = 0)$, and substitute it to (C.9), resulting in our final solution

$$
\begin{aligned}
\rho_s(s, k, q) =& \frac{A_{22}\rho_g^0 - A_{12}\rho_s^0}{\det(A)} + \frac{rA_{22}(A_{r,22}\rho_g(t = 0, k, k) - A_{r,12}\rho_s(t = 0, k, k))}{\det(A)\det(A_r)} \\
&+ \frac{1}{\det(A)\det(A_r)} \cdot \frac{A_{12}\det(A_r) + rA_{22}A_{r,12}}{A_{12}^+ \det(A_r) + rA_{22}^+ A_{r,12}} \cdot \Big(-\rho_g^{0,+}A_{22}^+\det(A_r) \\
&- \rho_g(t = 0, k, k)rA_{22}^+ A_{r,22} + \rho_s^{0,+}A_{12}^+\det(A_r) + \rho_s(t = 0, k, k)rA_{22}^+ A_{r,12}\Big).
\end{aligned}
\tag{C.13}
$$

Given our particular assumption of microtubule nucleation (C.2) and (C.3), we have derived the full solution for $\rho_g(s, k, q)$ written as (C.13). The solution for $\rho_s(s, k, q)$ may be derived similarly. These solutions directly correspond to the plus end density solutions $C_g(s, k)$ and $C_s(s, k)$. Direct experimental measurements are available for $C_g(t, x_+)$. As we are primarily interested in the velocity at which the front of plus ends advance in the long time limit, we proceed with our analysis focusing on the behavior of $C_g(t, x_+)$.

C.4 Aster expansion velocity and critical nucleation rate

C.4.1 Dispersion relations for $C_g(t, x_+)$

We wish to determine the velocity at which the aster expands. To the solution we found in (C.7), we apply the inverse Laplace transform $s \to t$,

$$C_g(t, k) = \frac{1}{2\pi i} \int_{\gamma - i\infty}^{\gamma + i\infty} e^{st} ds \, C_g(s, k)$$
$$= \sum \text{Res} \, C_g(s(k_j), k_j) \, e^{s(k_j)t}$$

where the subscript j specifies the different poles in $C_g(s, k)$. Further, we apply the inverse Laplace transform $k \to x_+$,

$$C_g(t, x_+) = \frac{1}{2\pi i} \int_{\gamma - i\infty}^{\gamma + i\infty} e^{x_+ k} dk \, C_g(t, k)$$
$$= \frac{1}{2\pi i} \int_{\gamma - i\infty}^{\gamma + i\infty} dk \sum \text{Res} \, C_g(s(k_j), k_j) \, e^{s(k_j)t} e^{x_+ k_j}$$

Finally, we transform the spatial variable to the right moving reference frame $z = x_+ - Vt$ with $V > 0$,

$$C_g(t, z) = \frac{1}{2\pi i} \int_{\gamma - i\infty}^{\gamma + i\infty} dk \sum \text{Res} \, C_g(s(k_j), k_j) \, e^{s(k_j)t} e^{(z + Vt)k_j}$$
$$= \frac{1}{2\pi i} \int_{\gamma - i\infty}^{\gamma + i\infty} dk \sum \text{Res} \, C_g(s(k_j), k_j) \, e^{k_j z} e^{(s(k_j) + k_j V)t}$$

We must evaluate this integral in the long time limit $t \to \infty$ which corresponds to the solution that describes the front of the expanding aster. Note that the integral takes the form of $\int f(k) e^{t(g(k))} dk$ where t is large. We follow 'steepest descent' or 'saddlepoint method' and approximate the integral to be dominated by the saddlepoint k^* for $g(k) = s(k) - kV$. We also impose a time invariance condition by requesting the real part of $g(k)$ to be zero at this point. In other words, the conditions

96

that yield the asympotic solution are:

$$\begin{cases} \dfrac{d(s(k) + kV)}{dk}\Big|_{k=k_j^*} = 0 \\ \mathrm{Re}\big(s(k_j^*) + k_j^* V\big) = 0 \end{cases} \qquad \text{(C.14)}$$

These two equations together with the equation that specifies the poles allow us to specify the pair of s and k that describes the shape and velocity of the expanding front (also called the 'dispersion relation', in which the shape and the velocity of the front are specified simultaneously).

We return to (C.13) and examine in which cases poles arise. Consider the following:

- $\det(A) = 0 \Leftrightarrow k = q_+$ is not a pole, since $A_{22} \to A_{22}^+$, $\rho_g(t = 0, k = q_+, k = q_+) = \rho_g^{0,+}$, etc. and the numerator becomes zero.

- $\det(A_r) = 0$ is not a pole, since the numerator becomes zero.
- $A_{12}^+ + \dfrac{r A_{22}^+ A_{r,12}}{\det(A_r)} = 0 \Leftrightarrow \det(A_r) = -r(s - v_s q_+ + f_{res})$ is a pole.

The only pole of the equation (C.13) specifies the asymptotic, traveling front solution of our system.

C.4.2 ASTER EXPANSION VELOCITY

The velocity of the aster expansion is derived from the conditions imposed by (C.14). Applying the ansatz that both s and k are real numbers, we rewrite these conditions as follows:

$$V = -\frac{d\,s(k)}{dk}\Big|_{k=k_i^*} = -\frac{s(k_i^*)}{k_i^*}$$

The pole is specified by $\det(A_r) = -r(s - v_s q_+ + f_{res}) \Leftrightarrow$

97

$$(s + v_g k + f_{cat} - r)(s - v_s k + f_{res}) - f_{res} f_{cat} = -r(s - v_s q_+ + f_{res}) \quad \Leftrightarrow$$

$$s^2 + [(v_g - v_s)k + f_{cat} + f_{res}]s + [-v_g v_s k^2 + (v_g f_{res} - v_s f_{cat} + v_s r)k - v_s r q_+] = 0$$
$$(\text{C.15})$$

Together with (C.11) which constrains q_+ given s, we have three equations and three unknowns s, k, q.

First, we combine equations (C.11) and (C.15) and find,

$$k = q \quad \text{or} \quad k = \frac{(v_g - v_s)s + (v_g f_{res} - v_s f_{cat} + v_s r)}{v_g v_s} - q. \qquad (\text{C.16})$$

The physical solution resulting in a right moving front ($s > 0$, $k < 0$, $q_+ > 0$) corresponds to the latter solution. Equating

$$\frac{dk}{ds} = \frac{v_g - v_s}{v_g v_s} - \frac{dq_+}{ds}$$

and

$$\frac{dk}{ds} = \frac{s}{k} = \frac{v_g - v_s}{v_g v_s} - \frac{v_g f_{res} - v_s f_{cat} + v_s r}{v_g v_s} \cdot \frac{1}{s}$$

gives us

$$\frac{dq_+}{ds} = \frac{q_+}{s} - \frac{v_g f_{res} - v_s f_{cat} + v_s r}{v_g v_s} \cdot \frac{1}{s}. \qquad (\text{C.17})$$

We differentiate (C.11) by $\frac{d}{ds}$ and solve for $\frac{dq_+}{ds}$,

$$\frac{dq_+}{ds} = \frac{(v_g - v_s)q_+ + 2s + f_{cat} + f_{res}}{2q_+ v_g v_s + (v_g - v_s)s + v_g f_{res} - v_s f_{cat}}. \qquad (\text{C.18})$$

Eliminating $\dfrac{dq_+}{ds}$ from (C.17) and (C.18),we obtain

$$q_+ = \frac{(v_g f_{res} - v_s f_{cat} + v_s r)(v_g f_{res} - v_s f_{cat}) + s(v_g^2 f_{res} + v_s^2 f_{cat} + v_s r(v_g - v_s))}{v_g v_s (v_g f_{res} - v_s f_{cat} + 2 v_s r)}.$$

We substitute this into (C.11), and choose the positive root for s.

$$
\begin{aligned}
s = \frac{1}{(f_{cat} - r)(v_g + v_s)(v_g f_{res} + v_s r)} \cdot \Big(& r(v_g f_{res} + v_s f_{cat})(v_g f_{res} - v_s f_{cat} + v_s r) \\
& + (v_g f_{res} - v_s f_{cat} + 2 v_s r)\sqrt{v_g v_s f_{cat} f_{res}(v_g f_{res} - v_s f_{cat} + v_s r)} \Big)
\end{aligned}
\tag{C.19}
$$

Using (C.16), we find

$$
\begin{aligned}
k = \frac{-1}{v_g(f_{cat} - r)(v_g + v_s)(v_g f_{res} + v_s r)} \cdot \Big(& r(v_g f_{res} - v_s f_{cat} + v_s r)(v_g(f_{res} - f_{cat} + r) + v_s r) \\
& + (v_g(f_{res} + f_{cat} - r) + v_s r)\sqrt{v_g f_{cat} f_{res} r(v_g f_{res} - v_s f_{cat} + v_s r)} \Big)
\end{aligned}
\tag{C.20}
$$

We require $r < f_{cat}$ as k_i^* diverges at $r = f_{cat}$. The velocity of the propagating front is

$$
\boxed{
V = -\frac{s}{k} = \frac{v_g(v_g f_{res} - v_s f_{cat})^2}{\left(\begin{aligned} & v_g(v_g f_{res} - v_s f_{cat})(f_{res} + f_{cat}) + (v_g + v_s)(v_g f_{res} + v_s f_{cat})r \\ & -2(v_g + v_s)\sqrt{v_g f_{cat} f_{res} r(v_g f_{res} - v_s f_{cat} + v_s r)} \end{aligned} \right)}
}
\tag{C.21}
$$

where the critical nucleation rate r_c is discussed in the proceeding section. Our expression is valid for the range $r_c \leq r \leq f_{cat}$. For $r < r_c$, the aster fails to expand and reaches a steady state size with limited radius. For $r > f_{cat}$, we expect some microtubules and the microtubules they nucleated to polymerize without ever experiencing a growth to shrinkage transition. In this scenario,

we expect the very periphery of the aster to expand at polymerization rate v_g, while the shape of the front evolves with time.

For the special case of $v_g f_{res} - v_s f_{cat} = 0$, we return to C.19 and C.20 and find the aster expansion velocity as:

$$V = \frac{v_g(v_g f_{res} + v_s f_{cat} + 2\sqrt{v_g v_s f_{cat} f_{res}})}{v_g(f_{res} - f_{cat} + r) + v_s r + \dfrac{v_g(f_{res} + f_{cat} - r) + v_s r}{v_s r}\sqrt{v_g v_s f_{cat} f_{res}}} \tag{C.22}$$

C.4.3 CRITICAL NUCLEATION RATE AND GAP VELOCITY

We define the critical nucleation rate r_c as the minimum value of nucleation r at which the system results in front propagation. As seen in C.21, the aster expansion velocity takes a real value as long as the content of the square root, $v_g f_{res} - v_s f_{cat} + v_s r$ is positive. The aster expansion velocity undergoes a classical saddle-node bifurcation. For $r < r_c$, there is no real solution for V, while, for $r > r_c$, a pair of stable and unstable fixed point solutions exists. Expression C.21 is the larger, stable solution of this pair. The critical nucleation rate is:

$$\boxed{r_c = f_{cat} - \frac{v_g}{v_s} f_{res}} \tag{C.23}$$

When $r = r_c$, aster expansion velocity takes a finite value, which we term the "gap velocity".

$$\boxed{V_{gap} \equiv \lim_{r \to r_c} V = \frac{-v_g v_s(v_g f_{res} - v_s f_{cat})}{v_g^2 f_{res} + v_s^2 f_{cat}}} \tag{C.24}$$

T HIS THESIS WAS TYPESET using L^ATEX, originally developed by Leslie Lamport and based on Donald Knuth's TEX. The body text is set in 11 point Egenolff-Berner Garamond, a revival of Claude Garamont's humanist typeface. The above illustration, *Science Experiment 02*, was created by Ben Schlitter and released under CC BY-NC-ND 3.0. A template that can be used to format a PhD dissertation with this look & feel has been released under the permissive AGPL license, and can be found online at github.com/asm-products/Dissertate or from its lead author, Jordan Suchow, at suchow@post.harvard.edu.